

Optical properties of coated black carbon aggregates: numerical simulations, radiative forcing estimates, and size-resolved parametrization scheme

Baseerat Romshoo¹, Thomas Müller¹, Sascha Pfeifer¹, Jorge Saturno², Andreas Nowak², Krzysztof Ciupek³, Paul Quincey³, and Alfred Wiedensohler¹

¹Leibniz Institute for Tropospheric Research, 04318, Leipzig, Germany

²PTB Physikalisch-Technische Bundesanstalt, 38116, Braunschweig, Germany

³Environment Department, National Physical Laboratory (NPL), Teddington, TW11 0LW, UK

Correspondence to: Baseerat Romshoo (baseerat@tropos.de)

Abstract. The formation of black carbon fractal aggregates (BCFAs) from combustion and subsequent aging involves several stages resulting in modifications of particle size, morphology, and composition over time. To understand and quantify how each of these modifications influences the BC radiative forcing, the optical properties of BCFAs are modelled. Owing to the high computational time involved in numerical modelling, there are some gaps in terms of data coverage and knowledge regarding how optical properties of coated BCFAs vary over the range of different factors (size, shape, and composition). This investigation bridged those gaps by following a state-of-the-art description scheme of BCFAs based on morphology, composition, and wavelength. The BCFAs optical properties were investigated as a function of the radius of the primary particle (a_0), fractal dimension (D_f), fraction of organics (f_{organics}), wavelength (λ), and mobility diameter (D_{mob}). The optical properties are calculated using the multiple sphere T-matrix (MSTM) method. For the first time, the modelled optical properties of BC are expressed in terms of mobility diameter (D_{mob}), making the results more relevant and relatable for ambient and laboratory BC studies. Amongst size, morphology, and composition, all the optical properties showed the highest variability with changing size. The cross-sections varied from $0.0001 \mu\text{m}^2$ to $0.1 \mu\text{m}^2$ for BCFA D_{mob} ranging from 24 nm to 810 nm. It has been shown that MAC_{BC} and SSA is sensitive to morphology especially for larger particles with $D_{\text{mob}} > 100\text{nm}$. Therefore, while using the simplified core-shell representation of BC in global models, the influence of morphology on radiative forcing estimations might not be adequately considered. The Ångström absorption exponent varied from 1.06 up to 3.6 and increased with the fraction of organics (f_{organics}). Measurement results of $AAE \gg 1$ are often misinterpreted as biomass burning aerosol, it was observed that the AAE of purely black carbon particle can be $\gg 1$ in the case of larger BC particles. The values of the absorption enhancement factor (E_λ) via coating were found between 1.01 and 3.28 in the visible spectrum. The E_λ was derived from Mie calculations for coated volume equivalent spheres, and from MSTM for coated BCFAs. Mie calculated enhancement factors were found to be larger by a factor of 1.1 to 1.5 than their corresponding values calculated from the MSTM method. It is shown that radiative forcings are highly sensitive towards modifications in morphology and composition. The black carbon radiative forcing ΔF_{TOA} (Wm^{-2}) decreases up to 61% as the BCFA becomes more compact, indicating that the global model calculations should account for changes in morphology. A decrease of more than 50% in ΔF_{TOA} was observed as the organic content of the particle increase up to 90%. The changes in the ageing factors (composition and morphology) in tandem result in an overall decrease in the ΔF_{TOA} . A parameterization scheme for optical properties of BC fractal aggregates was developed, which is applicable for modelling, ambient and laboratory-based BC studies. The parameterization scheme for the cross-sections (extinction, absorption, and scattering), single scattering albedo (SSA), and asymmetry parameter (g) of pure and coated BCFAs as a function of D_{mob} were derived from tabulated results of the MSTM method. Spanning over an extensive parameter space, the developed parametrization scheme showed promisingly high accuracy up to 98% for the cross-sections, 97% for single scattering albedos (SSA), and 82% for asymmetry parameter (g).

1. Introduction

Black carbon (BC), also called light-absorbing carbon (LAC), is produced from incomplete combustion of fossil fuels, biomass, and biofuels, and is reported to be the second largest contributor to global warming after CO_2 with the global forcing estimates ranging between 0.4 to 1.2 W/m^2 (Ramanathan and Carmichael, 2008). It has been found that the annual anthropogenic BC emissions have increased from 6.6 to 7.2 tera-grams during 2000-2010 (Klimont et al., 2017). Moreover, due to rapid urbanization in many developing regions like China, South Asia, South East Asia, the total aerosol mass constitutes of a significantly large portion of BC (Kumar et al., 2018; Bond

53 et al., 2007; Wiedensohler et al., 2002; Madueno et al., 2019, 2020). In addition to the warming effect, BC also
54 decreases snow albedo (Doherty et al, 2010), causes adverse health effects (Janssen et al., 2011), and lowers
55 visibility (Wang et al., 2020).

56 Optical properties of BC are of scientific interest because they allow conclusions to be drawn on the nature of
57 the particles and to investigate their radiative impacts (Liu et al., 2015; Safai et al., 2015). After its emission into
58 the atmosphere, BC particles undergo various changes in shape, size, and composition (Fierce et al., 2013). In the
59 early stages of formation, BC particles consist of loosely bound agglomerates made of numerous small spherules,
60 which collide to form strongly bound chain-like aggregates (Michelsen et al., 2017). Depending upon the
61 atmospheric conditions after emission, irregularly shaped primary spherules provide active sites for the
62 deposition of water vapour which causes changes in the hygroscopicity of the particles (Petzold et al., 2005; Peng
63 et al., 2017,). In addition to this, different by-products of combustion like organic vapours are deposited around
64 the particles (Siegmann et al., 2002; Rudich et al., 2007). These processes lead to the formation of coatings on
65 BC cores (Bond et al., 2006) and reshaping of the BC particles into more spherical structures (Abel et al., 2003).
66 With the BC particles becoming more compact, an increase in the extinction cross section is observed (Liu et al.,
67 2012). It was theoretically shown in clusters of absorbing spherules that the change in the optical cross-sections
68 with an increasing number of spherules (aggregation) is strongly dependent on the morphology (Berry and
69 Percival, 1986). Laboratory and ambient studies also show changes in the optical properties of BC with an
70 increasing volume of organic coating (Shiraiwa et al., 2010; Cheng et al., 2009). Even though the organic coating
71 is less absorbing by nature, but an increase in the absorption cross section is observed due to the lensing effect
72 (Zhang et al., 2018; Zanatta et al., 2016, Saleh et al., 2015). Additionally, there exists a class of organic carbon
73 (OC) with light absorbing properties, known as brown carbon, strongly absorbing solar radiation in the blue and
74 near-ultraviolet spectrum (Fleming et al., 2020; Feng et al., 2004; Chakrabarty et al., 2010; Chen and Bond, 2010).
75 Numerical modelling has been proven to be helpful in better understanding the effect of the changes that BC
76 particles undergo on their optical properties (Scarnato et al., 2013; Kahnert, 2010; Smith and Grainger, 2014).
77 The advantage of the modelling studies is the ability and flexibility they offer to simulate BC particles of desired
78 size, shape, and composition, hence improving our understanding of BCFAs at the micro-physical level.

79 The representation of the simulated BC particle plays an essential role in their numerically derived optical
80 properties. The assumption of BC particles as spheres is widely used by atmospheric scientists, especially in the
81 field of climate modelling (Stier et al., 2004; Ma et al., 2011; Düsing et al., 2018;). In the case of aged BC, it is
82 commonly considered that a spherical BC core is encapsulated inside another sphere representing the coating.
83 This morphology is used in the core-shell Mie theory (Bohren and Huffman, 1983) for obtaining the optical
84 properties of such particles. Even though this method is simple, it might result in larger discrepancies when
85 compared to the actual measurements (Wu et al., 2018). Mie theory also overestimates absorption for core-shell
86 configuration of BC particles in the visible range of light (Adachi et al., 2010). It was shown that the ratio of non-
87 BC to BC components plays an important role in determining the performance of different methods used for
88 simulating the BC optical properties (Liu et al., 2017). Electron microscopy results of the samples from laboratory
89 and ambient measurements of BC (Ouf et al., 2016; Dong et al., 2018) showed that the BC particles consist of
90 agglomerates made up of numerous primary particles. It has been observed that these particles show self-similarity
91 when viewed over a range of scales, which is an important characteristic of fractals (Forrest and Witten, 1979).
92 This makes BC particles suitable to be termed as black carbon fractal aggregates (BCFAs), and is used as such
93 throughout this study.

94 Discrepancies due to Mie theory have caused an increasing interest in the simulation of the BC optical
95 properties assuming a more realistic fractal morphology. A size-dependent empirical formula for the optical
96 properties of BCFAs was derived for the wavelength range from 200nm up to 12.2 μ m (Kahnert et al., 2010). The
97 optical properties of pure BCFAs, i.e., without any coating, were investigated by Smith and Grainger (2014),
98 further developing a parametrization for optical properties of pure BCFAs with respect to the number of primary
99 particles (N_s). A method to estimate the optical properties BCFAs was proposed using the machine learning model
100 'support vector machine' (Luo et al., 2018). Empirical equations on the BC Ångström absorption exponent (AAE)
101 were derived for different BC morphologies (Liu et al., 2018). A database containing optical data was developed
102 that includes the aggregation structure, refractive index, and particle size of BCFAs (Liu et al., 2019).

103 Various ambient and laboratory studies have emphasized the role of organic external coating in influencing the
104 BC absorption and scattering properties (Zhang et al., 2008, Ouf et al., 2016; Dong et al., 2018, Shiraiwa et al.,
105 2010). However, the previous modelling-based studies were not able to take into account the information about
106 the coating of the BCFAs. The reason for this could be that the time-consuming simulations make the
107 computational load for such a task substantially large. It was also pointed out that improved size-resolved datasets
108 and models for the light absorbing carbon (LAC) is required that includes observables like optical properties,
109 OC/BC ratio, burning phase or fuel types (Liu et al., 2020). Therefore, a size-resolved parametrization scheme for
110 optical properties of BCFAs including the external coating parameter is very important.

111 This investigation involved computationally intensive modeling aimed at understanding and quantifying the
112 changes that BCFAs and their optical properties undergo by simulating various cases of the BCFAs under an

113 elaborated systematic approach that is designed to span a wide parameter space. The coating parameter is
 114 quantified through the fraction of organics (f_{organics}). The BCFA cases are classified according to various f_{organics} ,
 115 morphologies, and wavelengths. This approach of categorization involving f_{organics} of BCFAs is aimed to bridge
 116 the gaps that are present in the modeled optical data from the previous studies. The optical properties were
 117 calculated using the T-matrix code (Mackowski et al., 2013) and the findings are presented and discussed with
 118 respect to the equivalent mobility diameter (D_{mob}) making it more relevant and comparable for laboratory, and
 119 ambient studies in which mobility spectrometers are often used for size classification.

120 The study highlights how modifications in the morphology and f_{organics} of BCFAs can further influence the BC
 121 radiative forcing. Finally, the parameterization scheme for optical properties (extinction, scattering, and
 122 absorption) of coated BCFAs was developed as a function of size for different morphologies, f_{organics} , and
 123 wavelengths.
 124

126 2. Methods

128 2.1 Morphology of BCFAs

129 The formation of BCFAs from combustion is a process involving several stages. Along with BC, a complex
 130 mixture of gas-phase organic compounds with a spectrum of molecular structures are co-emitted during
 131 incomplete combustion (Siegmann et al., 2002; Gentner et al., 2017). Depending upon the source of burning,
 132 different types of polycyclic aromatic hydrocarbons (PAHs) are considered to be the direct pre-cursors of BCFAs
 133 (Bockhorn 2009). Small PAHs such as acetylene (C_2H_2) are attached to larger precursor PAHs resulting in the
 134 growth of these elementary structures. It is postulated that the nucleation of two large PAHs leads to the formation
 135 of small three-dimensional particles with diameters ranging from 1-2 nm (Calcote, 1981).
 136

137 Processes like surface growth and coagulation of gaseous phase molecules or PAHs leads to further growth of
 138 these particles. High-resolution transmission electron microscopy (TEM) images revealed these particles to be
 139 spherules up to the diameter of 10-30nm specific to the flame (Homann, 1967). These primary particles show a
 140 randomly ordered microstructure of graphite layers (Hess et al., 1969). Following the processes of nucleation and
 141 coagulation, the primary particles form larger BCFAs, which subsequently grow by aggregation (Sorensen, 2001).
 142 Following this concept of fractal morphology, a mathematical description of fractal aggregates was formulated
 143 (Mishchenko et al., 2002) by:
 144

$$145 N_s = k_f \left(\frac{R_g}{a_0} \right)^{D_f}, \quad (1)$$

146 where, a_0 is the radius of primary particles, N_s is the number of primary particles, D_f is the fractal dimension, and
 147 k_f is a fractal pre-factor. R_g is the radius of gyration, which characterizes the spatial size of the aggregate. It is
 148 defined as root means square (rms) distance of the aggregate from its geometrical center by:
 149

$$151 R_g^2 = \frac{1}{N_s} \sum_{i=1}^{N_s} (r_i - r_o)^2, \quad (2)$$

152 where, r_i is the position vector of the i^{th} primary particle, and r_o is the position vector of the center of mass of
 153 an aggregate with radius of gyration R_g .

154 The size of a BCFA is determined by two parameters, the radius of the primary particle (a_0) and number of
 155 primary particles (N_s). Both are sensitive to the emission source. BCFAs originating from the combustion of
 156 biomass have a radius of the primary particle varying between 15- 25 nm (Chakrabarty et al., 2006). On the other
 157 hand, emissions from aircraft turbines comprise of primary particles with a radius of 5 nm (Liati et al., 2014).
 158 Aggregates emitted from diesel engines have a radius of the primary particle varying between 10 nm and 12 nm
 159 (Guaricero et al., 2018). Some experimental studies indicate that in the atmosphere, the radius of the primary
 160 particle is polydisperse in nature varying from 10-100nm (Bescond et al. 2014). Following these studies, Liu et
 161 al., 2015 reported differences in the optical properties of BCFAs due to the monodisperse and polydisperse
 162 distribution of the radii of the primary particles. Contrarily, Berry and Percival (1986) showed that light absorption
 163 measurements are insensitive to the radii of the primary particles. Additionally, Kahnert (2012b) pointed out that
 164 insensitivity is present when the radii of the primary particle fall in the range of 10 – 25nm. For the sake of
 165 simplicity, aggregates of monodisperse primary particle size were used in this study.
 166

167 Further, the reshaping of BCFAs into collapsed, sphere-like structures while ageing can be described by the
 168 fractal dimension (D_f) (Sorensen, 2001). The value of D_f increases as an aggregate reshapes into a more spherical
 169 particle. A D_f of 3 being the value for a sphere, whereas D_f of 1 represents an open-chain like aggregate. In the
 170 early stages of their formation, BCFAs have a fractal dimension (D_f) between 1.5 and 1.9 (China et al., 2014;
 171 Wentzel et al., 2003). However, as a consequence of the atmospheric aging, the aggregates transform from being

172 bare to partly coated, embedded in coatings. In this case, the fractal dimension can go up to 2.2 (Wang et al.,
 173 2017). The exposure to humidity and coatings can collapse the BCFA into a structure having even a larger fractal
 174 dimension up to 2.6. (Zhang et al., 2008; Bambha et al., 2013). Hence, studying BC particles under the assumption
 175 of aggregate morphology provides a wider range of parameter space (particle size, primary particle size, and
 176 morphology). This is limited to only particle size in case of spherical assumptions.

177 Aggregates are formed from the random motion of a cluster meeting cluster (Sorensen 2001). If the probability
 178 of sticking is considered 1, the process of formation is called the diffusion-limited cluster aggregation (Witten and
 179 Sander, 1983). Following this principle, Diffusion-limited algorithms (DLAs) have been developed, which
 180 include cluster-cluster aggregation (CCA) (Thouy and Julien, 1994) and particle-cluster aggregation (PCA)
 181 methods (Hentschel, 1984). In this study, the tunable diffusion limited aggregation (DLA) software developed by
 182 Woźniak (2012) was used, which iteratively adds the primary particle one by one, preserving the fractal
 183 parameters at each step.

185 2.2 Description scheme of the simulated BCFA's

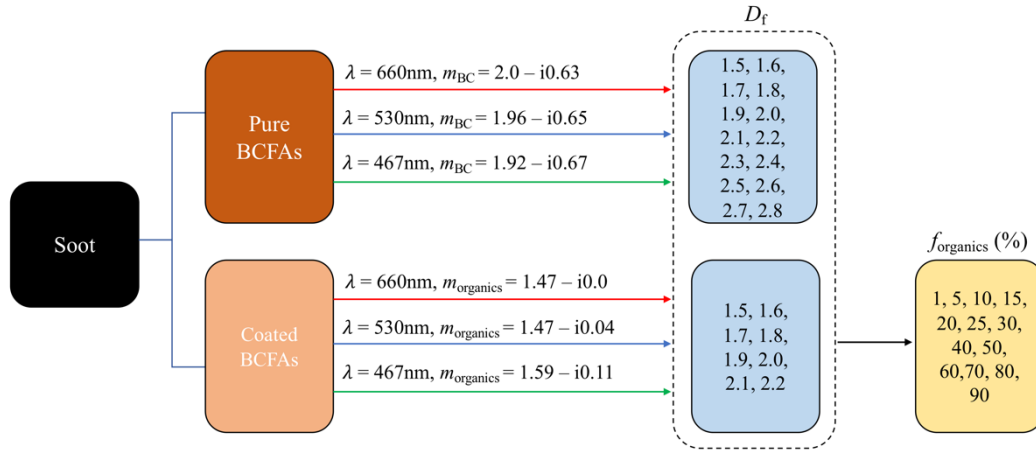
186 Previous modelling studies (Kahnert, 2010; Smith and Grainger, 2014) investigated the optical properties of pure
 187 BCFA's i.e., without any coating. From the simulated optical properties, parametrization for pure BCFA's with
 188 respect to the number of primary particles at various fractal dimensions and wavelengths were given (Smith and
 189 Grainger, 2014). Ouf et al. (2016) conducted Near Edge X-ray Absorption Fine Structure (NEXAFS) analysis on
 190 BC produced from a diffusion flame-based mini-CAST burner and found that organics (by-products of the
 191 combustion) get attached to the edge of graphite crystallites without changing the inner structure of the core. This
 192 laboratory result can be simulated for coated BC in radiative modeling studies by assuming a spherical coating
 193 around each individual primary particle of a BC aggregate (Luo et al., 2018). It must be noted that the focus of
 194 our study is on BCFA's with coatings consisting of non-absorbing organics. If a brown carbon coating was to be
 195 included in the study, information and extra computational time regarding their refractive indices was needed.
 196 Unfortunately, due to the time-consuming nature of simulations, the generated database could not include BCFA's
 197 with brown carbon coating.

198 For the sake of simplicity and computational limitations, this representation of coated BC shown in Fig. 2
 199 (bottom panel) was chosen for the entire study. In order to simulate such BC aggregates with individually coated
 200 primary particle, the inner radius of the primary particle (a_i) is fixed to 15 nm. Whereas the outer radius of the
 201 primary particle (a_o) consisting of the organics, is varied from 15.1nm to 30nm with the fraction of organics
 202 ($f_{organics}$) changing from 1% to 90% respectively. The relationship between the outer radius of the primary particle
 203 (a_o), the inner radius of the primary particle (a_i), and the fraction of organics ($f_{organics}$) is shown below:

$$206 \frac{4}{3}\pi a_i^3 = (1 - f_{organics}) \frac{4}{3}\pi a_o^3 \quad . \quad (3)$$

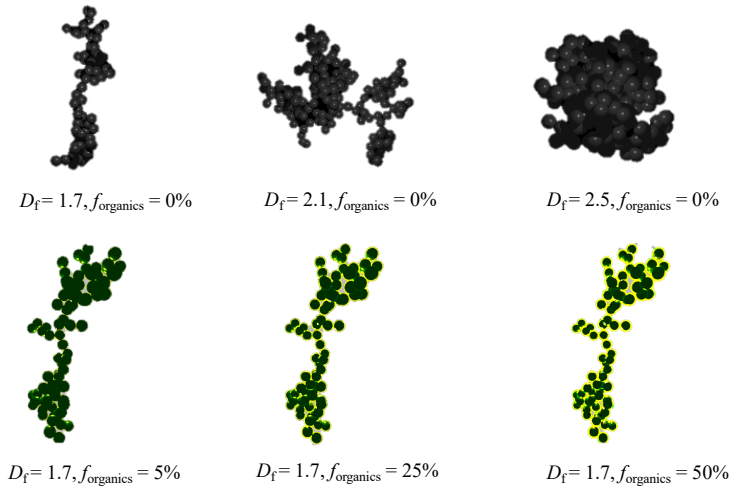
207 It must be noted that when the fraction of organics ($f_{organics}$) is larger than 80% and the morphology of the aggregate
 208 becomes compact, using this coated BC representation results in a practically unrealistic particle (randomly
 209 immersed BC primary particles in a spherical coating structure). Therefore, both the composition and morphology
 210 of the aggregate play a role while choosing the representation for coated BC. Keeping the above facts in mind,
 211 we have limited the use of this coating model only for coated BCFA's with fractal dimension D_f below 2.2. In such
 212 cases, where the BC aggregate does not have a completely compact structure, the results are expected to be reliable
 213 (Luo et al., 2018). Moreover, Kahnert et al., 2017 compared the coating model (closed-cell model) used in this
 214 study to a realistic model, which showed good comparability.

215 Luo et al., 2018 kept the overall size of aggregates constant to study the sensitivity of optical properties at
 216 various number of primary particles (N_s) and vice-versa. In our study, the size of the BC aggregates is increased
 217 gradually studying the subsequent changes in the optical properties. The optical properties of BC aggregates were
 218 calculated for various cases, following a well-designed description scheme summarized in Fig. 1. All the optical
 219 properties are calculated at three wavelengths in the visible range i.e., 467nm, 530nm and 660nm. The values are
 220 chosen following the availability of refractive index at these specific wavelengths from Kim et al, 2015. For pure
 221 BC aggregates, the optical properties were calculated for $1.5 \leq D_f \leq 2.8$ in steps of 0.1. In case of the coated BC
 222 aggregates, the optical properties are calculated at the above-mentioned wavelengths for $1.5 \leq D_f \leq 2.2$ in steps of
 223 0.1, and for $1\% \leq f_{organics} \leq 90\%$ in increments of 5%. The approach of assuming a spherical coating around each
 224 individual BC primary particle results in an unlikely structure for coated BCFA's with $D_f > 2.2$, hence those cases
 225 were omitted in this study. Fig. 2 shows a few of the aggregates from the classification at a fixed D_f and $f_{organics}$.
 226 The large dataset obtained from the classification helped in further developing the comprehensive parametrization
 227 scheme.



229
230
231

Figure 1. The description scheme of black carbon fractal aggregates (BCFAs) adopted in this study.



232
233
234
235

Figure 2. Examples of black carbon fractal aggregates (BCFA) with 200 primary particles, and varying D_f and $f_{organics}$.

236
237
238
239

In each case of the mentioned classification, the size of the BCFA is changed by incrementing N_s with 5% and rounded to an integer value, starting from 1 up to 1000. It must be noted that in the results, the size of the BCFA is expressed in terms of mobility diameter (D_{mob}) instead of the number of primary particles (N_s) using the simple conversion developed by Sorensen (2011) given below:

240
241
242

$$D_{mob} = 2a_0(10^{-2x+0.92})N_s^x \quad (4)$$

243
244
245

where, x is the mobility mass scaling exponent given by $x = 0.51Kn^{0.043}$ with $0.46 < x < 0.56$ having an estimated error of ± 0.02 (Sorensen, 2011). Kn is the Knudsen number, which is the ratio of the molecular free path to the agglomerate mobility radius.

246
247
248
249

The conversion formula given in (4) is well founded over the entire range, spanning from the continuum to free molecular regime. Using pre-calculated values of x , the mobility diameter (D_{mob}) is derived for the entire dataset. The relationship between derived mobility diameter (D_{mob}), number of primary particles (N_s) and volume equivalent diameter (D_{equ}) for a case of pure BCFA with $a_0 = 15$ nm is shown in Fig. 3.

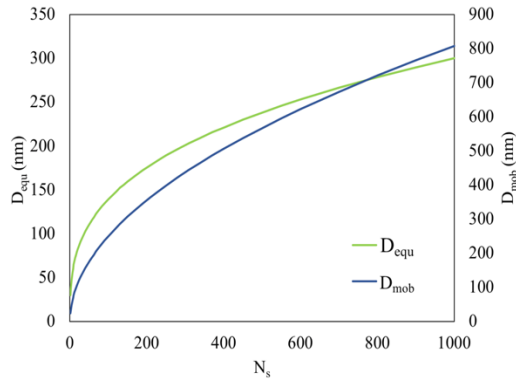


Figure 3. Relationship between mobility diameter (D_{mob}), number of primary particles (N_s) and volume equivalent diameter (D_{equ}) for pure BCFA with $a_0 = 15\text{nm}$.

BC has a refractive index fairly wavelength independent in the visible and near-visible spectrum range (Bond and Bergstrom., 2006). There are modelling studies which assume a wavelength independent refractive index of $m = 1.95 + 0.79i$ for BC over the visible spectrum range (Smith and Grainger., 2014; Luo et al., 2018). For organic carbon, the imaginary part of the refractive index (m_i) is highly wavelength dependent at the shorter wavelengths in the visible and ultraviolet (UV) wavelengths (Moosmüller et al., 2009; Alexander et al., 2008). Contrary to other studies, Kim et al., 2015 concluded that BC shows a fair amount of wavelength dependency, and provided refractive indices for BC and organics in the visible spectrum. Following his study, the real (m_r) and imaginary (m_i) part of the refractive indices used for BC and organics at different wavelengths in this study are summarized in table 1.

Table 1. Refractive indices (m_r and m_i) of BC and organics at various wavelengths in the visible range (Kim et al., 2015) used in this study.

Parameter	Wavelength (nm)		
	467	530	660
m_{r_BC}	1.92	1.96	2.0
m_{i_BC}	0.67	0.65	0.63
$m_{r_Organics}$	1.59	1.47	1.47
$m_{i_Organics}$	0.11	0.04	0

2.3 Optical properties from Multi-Sphere T-matrix Method (MSTM)

Multi-sphere T-matrix Method (MSTM) consists of an algorithm for calculating the time-harmonic electromagnetic properties of a set of arbitrary spheres (Mishchenko et al., 2004; Mackowski and Mishchenko, 2011). The MSTM version 3.0 (Mackowski et al., 2013) calculates the optical properties for fixed and random orientations, the latter being used in this study. MSTM code can calculate the optical properties of coated BCFA aggregates involving nested spheres with the condition that there should be no intersecting surfaces of individual primary particles. Radius, and positions vectors of the inner and outer primary particle of the BCFA are obtained from the tunable DLA software (Woźniak, 2012) which is coupled to the MSTM code.

The optical properties of the aggregates were modelled at three wavelengths, i.e., 467, 530, and 660 nm. At the wavelengths of 660nm and 530nm, the optical properties from MSTM code are obtained for $1 \leq N_s \leq 1000$. Because of the increasing processing time of the MSTM code at lower wavelengths, the calculations are limited to $1 \leq N_s \leq 500$ for a wavelength of 467nm.

For reference purposes, the optical properties were also calculated using the Mie theory, and the absorption cross-section from Rayleigh-Debye-Gans (RDG) theory. For the Mie theory calculations, spheres with volume equivalent radius of aggregates were taken. In case of the coated aggregates, a concentric core-shell configuration was used (He et al., 2015). The RDG theory considers the primary particles in the aggregate as individual Rayleigh scatters, while ignoring the inter-particle scattering (Sorensen, 2001). Therefore, in the RDG theory, the total absorption cross-section of the aggregate (C_{abs}^{agg}) is the summation of the absorption cross-sections (C_{abs}^{pp}) of

289 individual primary particles (N_s). For a monodisperse distribution, the absorption cross-section from the RDG
 290 theory is given as :

$$291 \quad C_{abs}^{agg} = N_s C_{abs}^{pp} \quad (5)$$

294 2.4 Optical properties and simplified radiative forcing model

295
 296 The radiative parameters calculated from the model are briefly presented below. The MSTM code provides the
 297 extinction, absorption and scattering efficiency (Q), and the asymmetry parameter (g) of BCFA. The extinction,
 298 absorption and scattering cross-sections ($C_{ext/abs/sca}$) are further obtained as the product of efficiency (Q) and
 299 geometric cross-section (C_{geo}) by:

$$300 \quad C_{ext/abs/sca} = (Q_{ext/abs/sca}) * C_{geo} \quad (6)$$

301
 302 In spherical objects with radii (R), the geometric cross-section (C_{geo}) is related to the radius by:

$$303 \quad C_{geo} = \pi R^2 \quad (7)$$

304
 305 Therefore, for a BCFA, the cross-sections ($C_{ext/abs/sca}$) with volume equivalent radius (R_v) are defined as follows:

$$306 \quad C_{ext/abs/sca} = Q_{ext/abs/sca} \pi R_v^2 \quad (8)$$

307
 308 The Volume equivalent radius (R_v) is calculated by:

$$309 \quad R_v = a_o N_s^{\frac{1}{3}} \quad (9)$$

310
 311 The single scattering albedo (SSA) is the ratio of scattering efficiency (Q_{sca}) and extinction efficiency (Q_{ext}),
 312 where Q_{ext} is the sum of absorption and scattering efficiency as shown below:

$$313 \quad SSA = \frac{Q_{sca}}{Q_{ext}} = \frac{Q_{sca}}{Q_{sca} + Q_{abs}} \quad (10)$$

314
 315 Values of ω varies from 0 for a purely absorbing particle to 1 for a completely scattering particle.

316 Mass absorption cross-section (MAC) is calculated from the ratio of absorption cross section (C_{abs}) and BC
 317 mass (m_{BC}) as:

$$318 \quad MAC = \frac{C_{abs}}{m_{BC}} = \frac{C_{abs}}{\frac{4}{3}\pi R_v^3 \rho_{BC}} \quad (11)$$

319
 320 where ρ_{BC} is the density of BC fixed to 1.8 g/cm³ (Bond and Bergstrom, 2006).

321 The wavelength dependence of light absorption, represented by the Absorption Ångström Exponent (AAE) is
 322 calculated using the absorption cross-section (C_{abs}) at the three wavelengths (λ) of 467, 530, and 660 nm. The
 323 AAE value is obtained by:

$$324 \quad C_{abs}(\lambda = 467, 530, 660) = b \lambda^{-AAE} \quad (12)$$

325
 326 where b is a constant.

327 The absorption enhancement factor (E_λ) is defined by the ratio of absorption cross section of coated BCFA
 328 (C_{abs}^{coated}) and pure BCFA (C_{abs}^{pure}) as shown below:

$$329 \quad E_\lambda = \frac{C_{abs}^{coated}}{C_{abs}^{pure}} \quad (13)$$

330
 331 This implies that the enhancement is given for particles of different total mass but the same BC mass.

332 To understand the atmospheric implication, the radiative forcing is estimated using a model for absorbing
 333 aerosols given by Chylek and Wong, 1995. The black carbon radiative forcing at the top of the atmosphere is
 334 calculated as:

335
 336
 337
 338
 339
 340
 341
 342
 343

$$\Delta F_{TOA} = -\frac{S_o}{4}(1 - N_{cloud})T^2 2\tau[(1 - a)^2\beta\omega - 2a(1 - \omega)] \quad (14)$$

where, S_o is the solar constant, N_{cloud} is the cloud fraction, T is the transmittance of the sky above the layer of aerosols, τ is the aerosol optical depth, β is the upward scattering function, a is the surface albedo, and ω is the single scattering albedo. From Sagan and Pollack, 1967, the upward scattering function β is calculated from the asymmetry parameter g by:

$$\beta = \frac{1}{2}(1 - g) \quad (15)$$

The model given by Chylek and Wong (1995) for the calculation of TOA forcing is a simplified version of the multiple reflection model (Haywood and Shine, 1995; Sheridan and Ogren, 1999) with some implicit approximations. It is important to note that this is an analytical model which can be useful to understand the sensitivities of radiative forcing to various parameters (Chylek and Wong, 1995; Lesins et al., 2002). The simplified version was used in this study to highlight the sensitivity of the TOA forcing towards the morphology and composition of BC. However, the model cannot be used to replace the accurate direct radiative forcing calculations.

360

361 **3 Results and discussion**

362

363 **3.1 Variability in optical properties due to randomized particle generation**

364

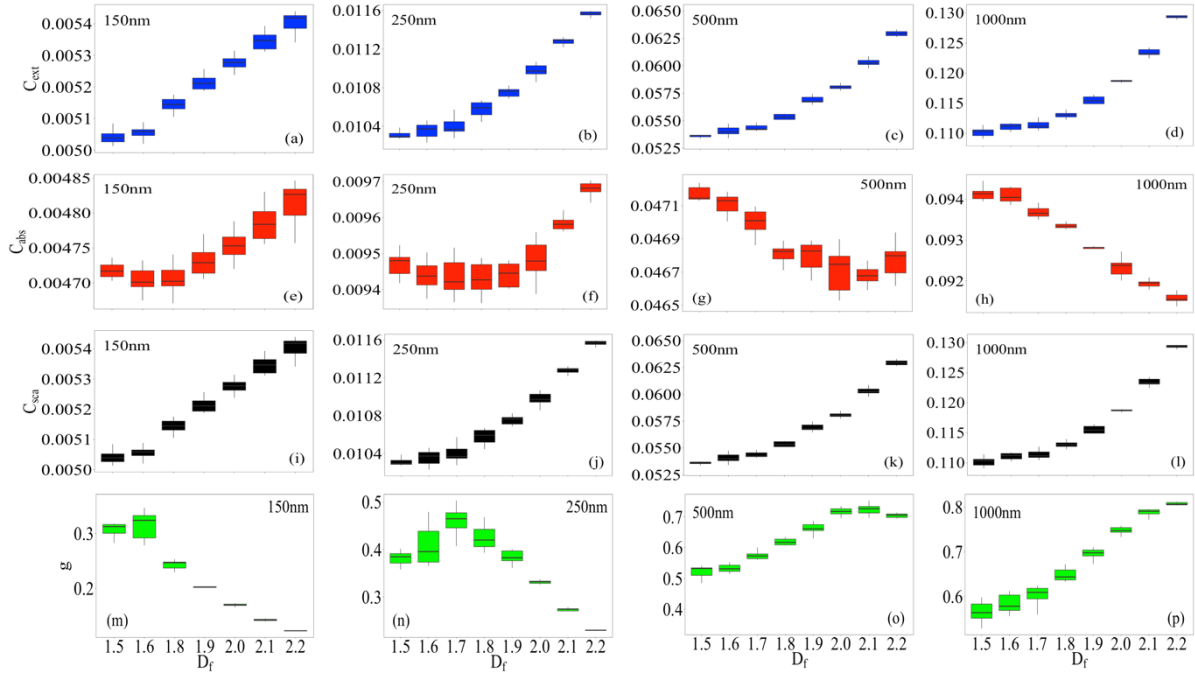
365 In the tunable DLA program, the user specified values of number of spheres (N_s), radius of the primary particle
 366 (a_o), and fractal dimension (D_f) are used to generate the fractal aggregate. This gives rise to a possibility of more
 367 than one representation of a fractal aggregate satisfying the same fractal dimension (D_f) i.e., randomized particle
 368 generation. The difference between the various representations being only the different positions of the primary
 369 particles constituting the aggregate. This further results in an uncertainty in the radiative results. Depending on
 370 the complexity, some studies averaged the radiative results over 5-10 representations (Wu et al., 2016; Luo et al.,
 371 2018), whereas others consider only a single representation (Smith and Grainger, 2014).

372 Considering the large dataset in this study, the option of taking an average of the multiple representations would
 373 be time-consuming. Therefore, the general uncertainty in optical properties for 30 representations of the pure
 374 BCFA is discussed. This is done for various cases of size (D_{mob}) and morphology (D_f). Fig. 4 shows the variability
 375 in the extinction cross-section C_{ext} (first row), absorption cross-section C_{abs} (second row), scattering cross-section
 376 C_{sca} (third row), and asymmetry parameter g (fourth row) as a function of D_f . The results were calculated at a
 377 wavelength of 660 nm for pure BCFA of D_{mob} values 150nm, 250nm, 500nm, and 1000nm increasing from left
 378 to right in the Fig. 4.

379 The uncertainty in the optical properties was studied for 30 representations of BCFA with the same value of
 380 the fractal dimension. The amount of variability in the optical property at each fractal dimension (x-axis) must be
 381 seen from the whiskers of the boxplot in Fig. 4. The sensitivity of the optical properties with respect to various
 382 fractal dimensions can be figured out from the amount of overlapping of the y-axis values between adjacent
 383 boxplots.

384 For extinction and scattering cross-sections (first and third row), the uncertainty is more pronounced at $D_f <$
 385 1.7. This is because of the overlapping of extinction and scattering cross-sections values at $D_f < 1.7$. The
 386 absorption cross-section (C_{abs}) shows the highest uncertainty towards various representations of a BCFA which
 387 can be seen from higher heights of boxplots in panel (e), (f), and (g) of the Fig. 4. Additionally, at 150 nm and
 388 250 nm, C_{abs} is seen to be less sensitive towards D_f ranging between 1.5 - 2. Whereas, for boxplots in panel (g)
 389 representing a 500nm BCFA, the C_{abs} values overlap for $D_f > 1.8$. It may be noted that the C_{abs} increases with D_f
 390 for smaller BCFA (panel (e) and (f)), whereas the opposite is true for larger BCFA (panel (g) and (h)) as also
 391 reported by Luo et al, 2018. This is further explained in detail in the section 3.3. The asymmetry parameter (g)
 392 shows a similar uncertainty trend to that of the extinction and scattering cross-sections i.e., lower variability but
 393 some overlapping at certain D_f seen in fourth row. In general, it is observed that the uncertainty of optical
 394 properties at larger sizes ($D_{mob} = 1000\text{nm}$; last column) is comparatively low. The standard deviation in the optical
 395 properties is averaged over size, and summarized for various cases of D_f in Table 2.

396



397
398
399
400
401
402
403
404
405
406
407
408
409
410

Figure 4. The variability in the optical properties at $\lambda = 660\text{nm}$ for 30 representations of pure BCFA with D_{mob} increasing (left to right). The panels show extinction cross-section C_{ext} (first row), absorption cross-section C_{abs} (second row), scattering cross-section C_{sca} (third row), and asymmetry parameter g (fourth row). The boxplots show the interquartile range between 75 - 25 percentile, with the center bar in the box indicating the median. The whiskers on the top and bottom of the boxplot mark the largest and smallest value within 1.5 times interquartile range.

Table 2. Summary of the variability (%) in the optical properties of pure BCFA. The variability of extinction cross-section C_{ext} , absorption cross-section C_{abs} , scattering cross-section C_{sca} , asymmetry parameter g , and single scattering albedo SSA are shown for fractal dimension (D_f) between 1.5 to 2.2. For each case, the resultant variability is an average over the sizes of 100, 250, 500, and 1000nm.

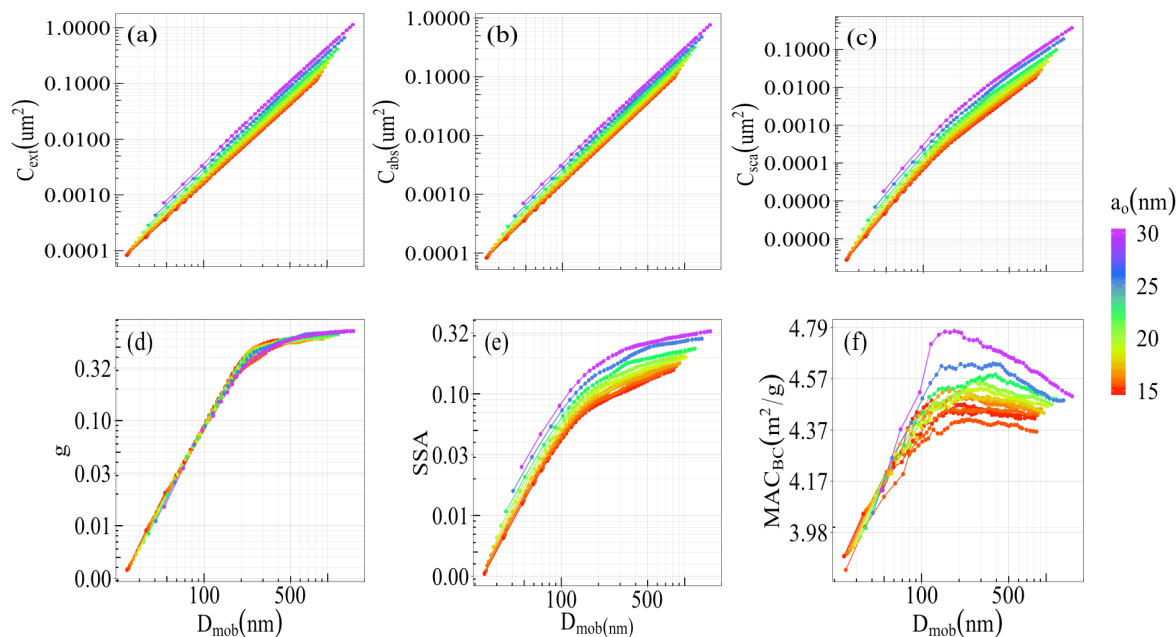
Optical property	Fractal dimension (D_f)							
	1.5	1.6	1.7	1.8	1.9	2	2.1	2.2
C_{ext}	0.54	0.75	0.65	0.56	0.54	0.46	0.73	0.73
C_{abs}	0.24	0.26	0.34	0.24	0.20	0.39	0.36	0.36
C_{sca}	4.68	5.90	4.68	3.25	2.68	1.52	2.97	2.97
g	5.81	5.24	4.32	2.90	1.76	1.45	3.36	1.56
SSA	4.20	5.29	4.09	2.71	2.17	1.17	2.29	2.29

411
412
413
414
415
416
417
418
419
420
421
422
423
424
425

3.2 Optical properties of BCFA at different radius of the primary particle

The absorption cross-section (C_{abs}) and BC mass absorption cross-section (MAC_{BC}) have been reported to be insensitive to radius of the primary particle (a_0) for a fixed particle volume (Kahnert, 2016b). Fig. 5 shows the optical properties of pure BCFA with the radius of primary particle (a_0) varying between 15nm and 30nm as a function of D_{mob} . The results were calculated for a wavelength of 660nm for pure BCFA with $D_f = 1.7$. The absorption cross-section C_{abs} showed in panel (b) increases by a factor of almost ten from a_0 equal to 15nm to 30nm. Since our results here are represented against D_{mob} instead of volume equivalent radius (R_{equ}), they are not expected to follow the findings of Kahnert, 2016b. The results with respect to the R_{equ} are provided in the Fig. S1 of the supplementary material, which follow the findings of Kahnert, 2016b. The asymmetry parameter shows the least dependency on a_0 as can be seen in panel (d). The single scattering albedo (SSA) and the BC mass absorption cross-section (MAC_{BC}) shown in panel (e) and (d) of the Fig. 5 show a larger increase at $a_0 > 20\text{nm}$ for the same D_{mob} . Acknowledging the effect of changing a_0 over the optical properties, for the sake of simplicity, in this study

426 the inner radius of the primary particle (a_i) was fixed to 15nm, and the outer radii of the primary particle (a_o) was
 427 increased with f_{organics} .
 428



429
 430 **Figure 5.** Optical properties of pure BCFA at various radii of primary particle (a_o) with respect to mobility
 431 diameter (D_{mob}): (a) extinction cross-section C_{ext} , (b) absorption cross-section C_{abs} , (c) scattering cross-section
 432 C_{sca} , (d) asymmetry parameter g , (e) single scattering albedo SSA , and (f) black carbon mass absorption cross-
 433 section MAC_{BC} at $\lambda = 660\text{nm}$.
 434

435 3.3 Dependency of BCFA optical properties on the morphology

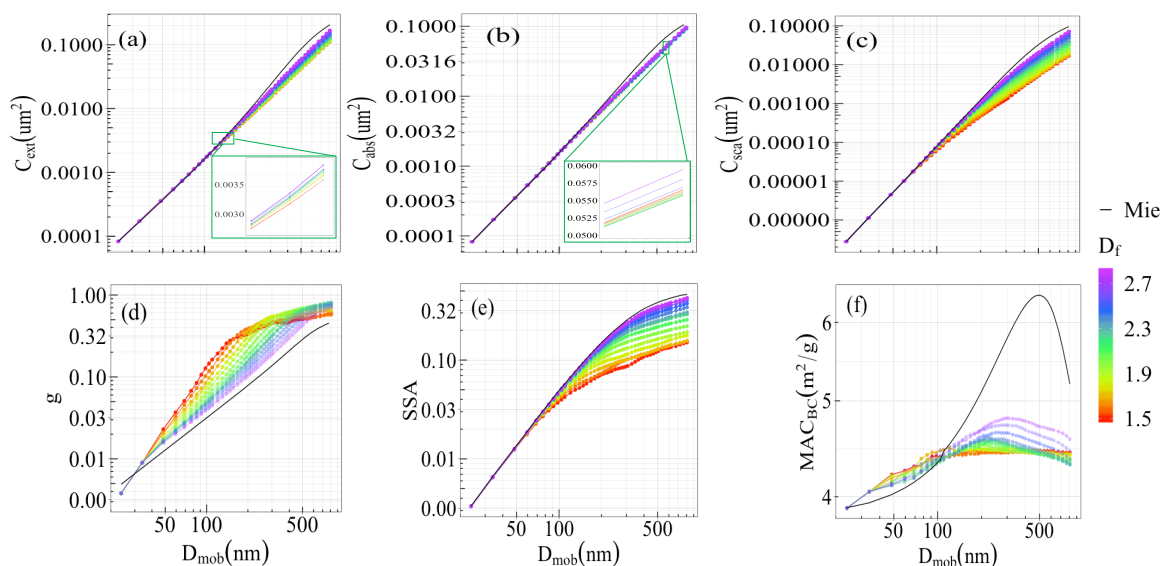
436
 437 Different optical properties as a function of changing D_{mob} , and D_f are shown in Fig. 6. The results were calculated
 438 for pure BCFA ($f_{\text{organics}} = 0$) at a wavelength of 660nm. The cross-sections (panel (a), (b), and (c)) show an
 439 increase with D_{mob} . The cross-sections vary from $0.0001\mu\text{m}^2$ to $0.1\mu\text{m}^2$ for BCFA D_{mob} ranging from 24nm to
 440 810nm. The extinction and scattering cross-sections are larger for higher D_f , suggesting an increasing coherent
 441 scattering for compact morphologies also reported by Smith and Grainger (2014). The dependency of the optical
 442 cross-section over the fractal dimension (D_f) was pointed out by Berry and Percival (1986) where the change in
 443 the cross-sections depends on whether the fractal dimension (D_f) is less than two or greater than two. The results
 444 from Mie calculations for a spherical particle ($D_f = 3$) follows the trend of the MSTM results as seen in the Fig.
 445 6.

446 For smaller BCFA, the absorption cross-section shows negligible dependence on D_f . With increasing size, the
 447 absorption cross-section decreases with D_f . This decrease can be interpreted as a shielding effect due to the
 448 primary particles on the surface of the aggregate. Further, with $D_f > 2.5$, the absorption cross-section increases
 449 with D_f showing the highest value for a spherical particle ($D_f = 3$). This may be caused by Mie resonances in larger
 450 BCFA. Earlier studies have also reported higher values for the sphere equivalent ($D_f = 3$) calculations of BCFA
 451 (Liu et al., 2018; Li et al., 2016).

452 The single scattering albedo ($SSA = C_{\text{sca}}/C_{\text{ext}}$) shown in panel (e) of Fig. 6 has values up to 0.42. The SSA also
 453 increases with D_{mob} and D_f , the latter is explained by the decreasing scattering in loosely packed BCFA. This is
 454 due to compact aggregates following a Rayleigh-like polarization curve (Gustafson and Kolokolova, 1999). The
 455 asymmetry parameter (g) (panel d) shows a range of values between 0 and 1 for values of D_{mob} values between
 456 24nm and 810nm. The asymmetry parameter is higher for chain-like BCFA with lower D_f , indicating larger
 457 forward scattering in asymmetrical structures also reported by Luo et al. 2018. When the BCFA grow larger. the
 458 rate of increase in g with size gradually decreases for lower D_f because of the scattering tending to the Rayleigh
 459 scattering regime.

460 Black carbon mass absorption cross-section (MAC_{BC}) values shown in panel (f) fall within the range of findings
 461 reported in the literature (Bond and Bergstrom, 2006). The MAC_{BC} increase with D_{mob} showing a peak at $D_{\text{mob}} \sim$
 462 250nm. The dependency of MAC_{BC} on D_f is similar to that of the absorption cross-section i.e., Mie resonances

463 contribute to the increase at higher D_f , explaining the large discrepancy between MSTM and Mie results for
 464 MAC_{BC} . The above results with respect to the R_{equ} are provided in the Fig. S2.



465 **Figure 6.** Optical properties of pure BCFA as a function of D_{mob} at various fractal dimension (D_f): (a) extinction
 466 cross-section C_{ext} , (b) absorption cross-section C_{abs} , (c) scattering cross-section C_{sca} , (d) asymmetry parameter g ,
 467 (e) single scattering albedo SSA , and (f) black carbon mass absorption cross-section MAC_{BC} at $\lambda = 660\text{nm}$.
 468 Radiative results from the Mie calculations are shown by the black line (panel a-f). The C_{abs} from the Rayleigh-
 469 Debye-Gans (RDG) theory is represented by a dash line (panel b).
 470
 471

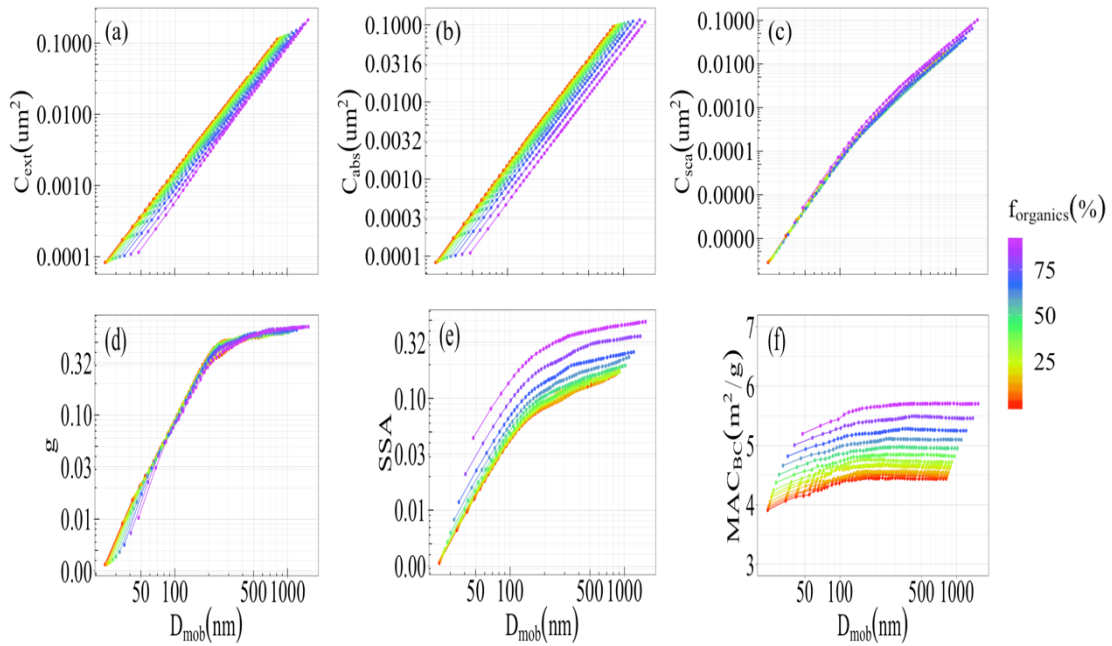
472 3.4 Dependency of BCFA optical properties on $f_{organics}$

473
 474 Figure 7 shows how the optical properties of BCFA are influenced by the increasing content of organics. The
 475 calculations were done for a BCFA of chain-like morphology with $D_f=1.7$ at a wavelength of 660nm. The results
 476 are shown as function of D_{mob} at various fractions of organics ($f_{organics}$). The extinction and absorbing cross-sections
 477 (Fig. 7a and 7b) decrease steadily with increasing $f_{organics}$ for constant mobility diameters because of the increasing
 478 less-absorbing volume fraction in the aggregate. The dependence on the asymmetry parameter g (Fig. 7d) on
 479 $f_{organics}$ is very small, meaning that g is more sensitive to morphology rather than composition. The single scattering
 480 albedo (SSA) increases with $f_{organics}$, and this is again because of the increasing fraction of less absorbing material.
 481 From the results of black carbon mass absorption cross-section (MAC_{BC}) values shown in Fig. 7f, a dominating
 482 dependence of BCFA on composition is seen, in comparison to size and morphology. Similar results for a compact
 483 BCFA of $D_f=2.2$ at a wavelength of 660nm can be found in the Fig. S4 of the supplementary material.
 484

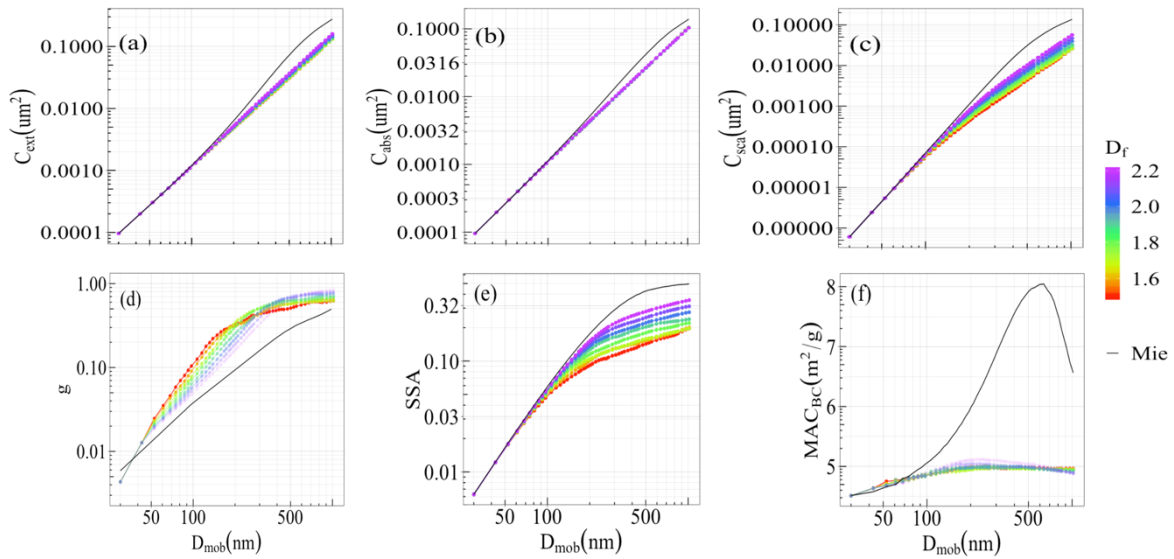
485 Figure 8 is similar to Fig.6 but shows the dependency of optical properties on the fractal dimension (D_f) for
 486 organic coated BCFA with $f_{organics}$ of 50% at the wavelength of 660nm. The cross-sections and asymmetry
 487 parameter show similar behaviour such as that of the pure BCFA. The SSA has an upper limit of 0.35 at $D_f=2.2$.
 488 Black carbon mass absorption cross-section (MAC_{BC}) is rather independent of D_f but values increase with coating
 489 by a factor of 1.2 for coated BCFA with $f_{organics}$ of 50% as shown in Fig. 7.

490 The gradually decreasing impact of the fractal morphology on the optical properties of coated BC particles was
 491 shown by Liu et al., 2017. In this study, it is seen in the case of a non-coated BC particle (Fig. 6c), the C_{sca} is more
 492 sensitive to the D_f , whereas, when the BC particles are coated (Fig. 7c, Fig 8c), the C_{sca} is less sensitive towards
 493 D_f and $f_{organics}$. It is observed that the C_{sca} and SSA (Fig. 8c, Fig. 8e) become more sensitive to D_f when the BCFA
 494 grows in size, therefore, the impact of the fractal morphology over the optical properties is also a function of
 495 particle size. Moreover, it must be noted that even though there is a decreasing impact of the fractal morphology
 496 on optical properties, parameters like C_{abs} , MAC_{BC} , and g showed significant variability towards changes of $f_{organics}$
 497 (Fig 7a, 7b, 7e, and 7f).

498 Global models use Mie theory for calculations of BC optical properties (Bond et al., 2013). The Mie theory
 499 considers BC as homogeneously mixed spheres, or as a core-shell configuration. The results of SSA , g , and MAC_{BC}
 500 in both Fig.6 and Fig.8 clearly demonstrate a significant influence of morphology. This is clearly seen from the
 501 difference between the coloured lines representing various morphologies of BC as aggregates, and the black solid
 502 line representing the result when BC is assumed as a core-shell. Therefore, the factor of changing morphology is
 503 not considered adequately when using the Mie theory for BC optical properties in global models.



504
 505 **Figure 7.** Optical properties of BCFA ($D_f = 1.7$) as a function of D_{mob} at various fraction of organics ($f_{organics}$):
 506 (a) extinction cross-section C_{ext} , (b) absorption cross-section C_{abs} , (c) scattering cross-section C_{sca} , (d) asymmetry
 507 parameter g , (e) single scattering albedo SSA , and (f) black carbon mass absorption cross-section MAC_{BC} at $\lambda =$
 508 660nm



509
 510 **Figure 8.** Optical properties of coated BCFA ($f_{organics} = 50\%$) as a function of D_{mob} at various fractal dimension
 511 (D_f): (a) extinction cross-section C_{ext} , (b) absorption cross-section C_{abs} , (c) scattering cross-section C_{sca} , (d)
 512 asymmetry parameter g , (e) single scattering albedo SSA , and (f) black carbon mass absorption cross-section
 513 MAC_{BC} at $\lambda = 660\text{nm}$.

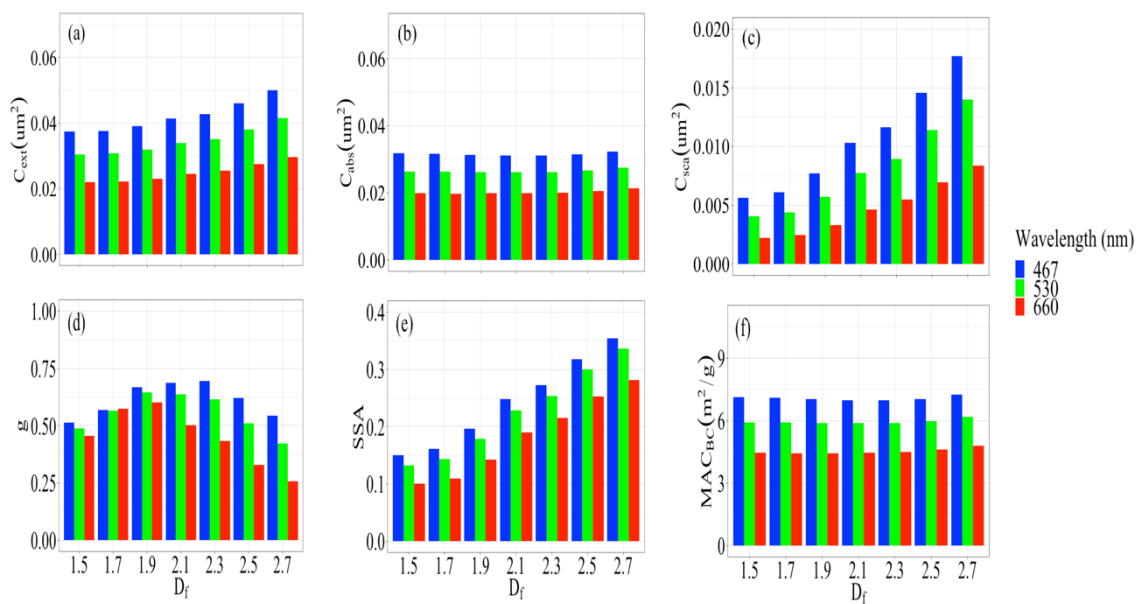
514 3.5 Dependency of BCFA optical properties on wavelength

515
 516 In the sections before, the dependency of BCFA optical properties on size, morphology, and composition were
 517 discussed. In this section, besides showing the spectral dependency of BCFA optical properties, it is also
 518 demonstrated how this dependency changes with morphology, and composition in the visible wavelength range.
 519

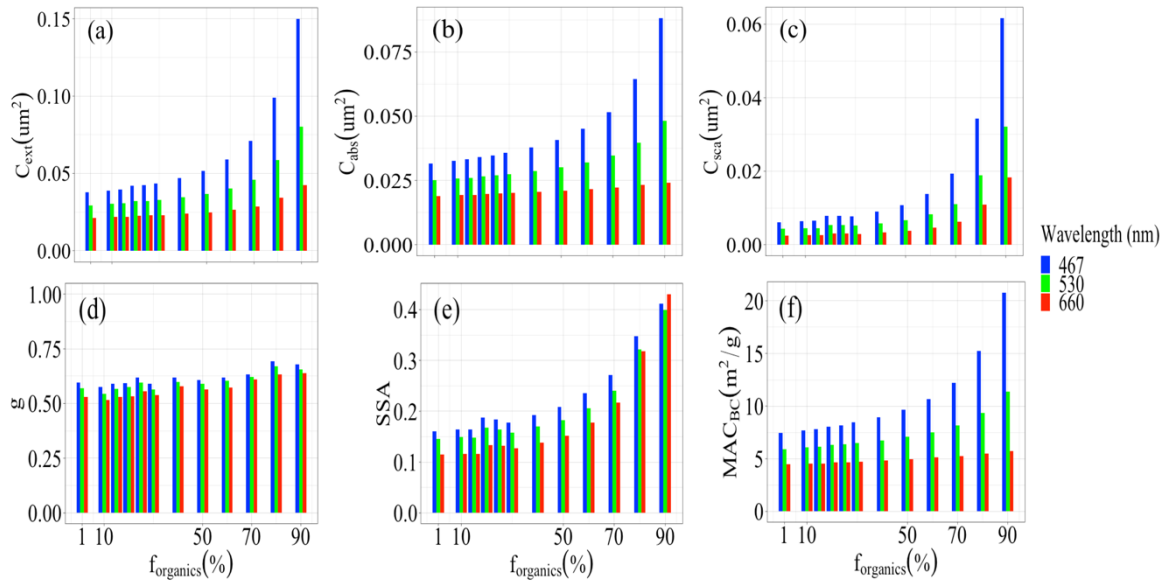
520 Figure 9 shows the changes in the pure BCFA's optical properties with wavelength (λ) at various morphologies
 521 represented by D_f . Pure BCFA's with fixed D_{mob} equal to 330nm were taken for this case to demonstrate the effect
 522 of morphology. All the optical properties show a decrease with λ in the visible range. Furthermore, it was studied
 523 whether the rate of decrease might vary for various morphologies. Fig. 9 show that the spectral dependency is
 524 insensitive to morphology for the absorption cross-section C_{abs} (panel (b)) and black carbon mass absorption cross-
 525 section MAC_{BC} (panel (f)). The spectral dependence of scattering cross-section C_{sca} (panel (c)) is seen to be
 526 somewhat sensitive towards changes in morphology. The highest sensitivity of spectral dependence to
 527 morphology was seen for the asymmetry parameter (g), dominant at higher D_f i.e., for compact aggregates.

528 Figure 10 is provided to illustrate how the spectral dependency of BCFA's changes with composition i.e.,
 529 fraction of organics ($f_{organics}$). For this case, BCFA's are considered with N_s and D_f equal to 200 and 1.7 respectively.
 530 It must be noted that the size of the BCFA's is also increasing with $f_{organics}$. Contrary to the results from Fig. 9, all
 531 the cross-sections (panel (a), (b), and (c)) and black carbon mass absorption cross-section MAC_{BC} (panel (f)) show
 532 a significant increase in the spectral dependency with $f_{organics}$. The spectral dependency of single scattering albedo
 533 SSA (panel (d)) shows a comparatively lower sensitivity towards $f_{organics}$, whereas it's nearly negligible for the
 534 asymmetry parameter (g) seen in panel (e). Additionally, the change in spectral dependency over the size is also
 535 shown in the Fig. S5 of the supplementary material.

536



537 **Figure 9.** Spectral dependency of the pure BCFA's optical properties ($D_{mob} = 330nm$) on fractal dimension (D_f):
 538 (a) extinction cross-section C_{ext} , (b) absorption cross-section C_{abs} , (c) scattering cross-section C_{sca} , (d) asymmetry
 539 parameter g , (e) single scattering albedo SSA , and (f) black carbon mass absorption cross-section MAC_{BC} . For the
 540 variability (%) in different cases of D_f refer to Table 2.
 541
 542



543
 544 **Figure 10.** Spectral dependency of coated BCFA optical properties ($N_s = 200$, $D_f = 1.7$) on fraction of organics
 545 (f_{organics}): (a) extinction cross-section C_{ext} , (b) absorption cross-section C_{abs} , (c) scattering cross-section C_{sca} , (d)
 546 asymmetry parameter g , (e) single scattering albedo SSA , and (f) black carbon mass absorption cross-section
 547 MAC_{BC} . For the variability (%) refer to the case $D_f = 1.7$ in Table 2.

548
 549

550 3.6 Ångström absorption exponent (AAE) and enhancement factors (E_λ)

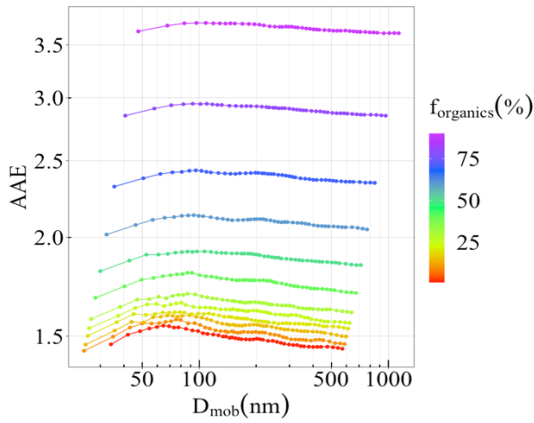
551

552 Figure 11 shows the Ångström absorption exponent (AAE) of a chain-like BCFA ($D_f = 1.7$) as a function of
 553 mobility diameter (D_{mob}), and increasing fraction of organics (f_{organics}). The AAE is derived from the slope of C_{abs}
 554 vs λ at 467, 530, and 660 nm as shown in Eq. (12). As expected, the AAE shows a straightforward dependency
 555 on the fraction of organics (f_{organics}). In this case, the values of AAE vary from 1.4 up to 3.6 with increase in f_{organics}
 556 from 1% until 90%. The variability in the modelled values of AAE may be attributed to the selection of the
 557 refractive indices and wavelengths (Liu et al., 2018). Similar result for the Ångström absorption exponent (AAE)
 558 of a more compact BCFA ($D_f = 2.2$) is provided in the Fig. S6. Additionally, the impact of morphology or fractal
 559 dimension (D_f) on the AAE for pure BCFA is shown in Fig. 12 with values ranging from 1.06 to 1.47. It can be
 560 observed that for smaller BCFA, the AAE increases as the BCFA becomes more compact, whereas for larger
 561 BCFA an opposite effect is seen. Fig. 11 and 12 could be interpreted as the ageing process of BC in the atmosphere
 562 focusing on changing composition and shape respectively.

563 Figure 13 shows the trend in absorption enhancement factors (E_λ) as a function of mobility diameter (D_{mob}) and
 564 increasing fraction of organics (f_{organics}) for a BCFA with $D_f = 1.7$. The top row shows the absorption enhancement
 565 factors calculated from the results of the MSTM code (E_{MSTM}^λ) whereas, the ones derived from the Mie
 566 calculations (E_{Mie}^λ) are displayed in the bottom row. In general, the Mie derived absorption enhancement factors
 567 are larger by a factor of 1.1 to 1.5. The enhancement results from both MSTM and Mie calculations are shown
 568 for three wavelengths i.e., 660, 530, and 467nm (right to left). There is an expected increase in the absorption
 569 enhancement factors as the wavelength decreases. The values of the modelled absorption enhancement factors
 570 follow the results from various ambient studies which measured enhancement factors ranging from 1.0 to 2.25 at
 571 wavelengths between 532nm to 678nm (Cappa et al., 2012; Cui et al., 2016; Wu et al., 2018).

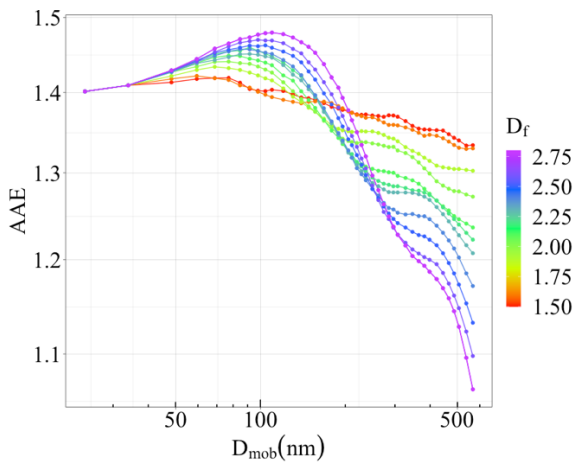
572 Liu et al., 2017 emphasized the role of the mass ratio of non-BC to BC on the performance of various methods
 573 used for simulating the scattering cross-section and enhancement factors of BC particles. In this study, it is shown
 574 that the Ångström absorption exponent (AAE) calculated from just the MSTM method can show variability of up
 575 to a factor of two with an increasing non-BC mass fraction larger than 90%. Similarly, it can be seen that the
 576 difference in the enhancement factors calculated from the core-shell theory and fractal assuming MSTM method
 577 can be up to by values between of 1.1 and 1.5.

578
 579



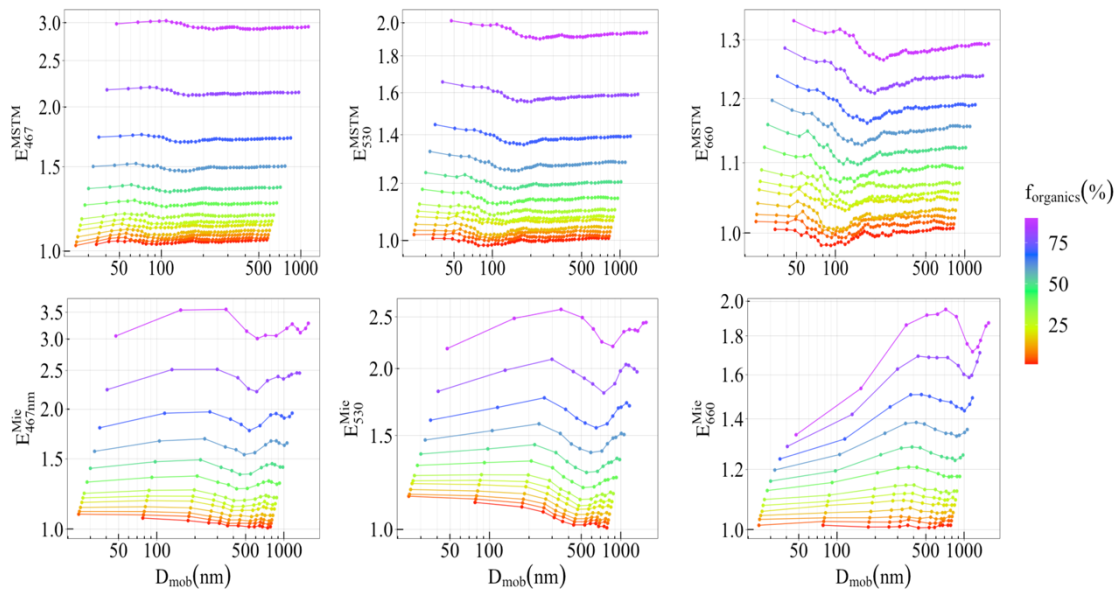
580
581
582
583
584

Figure 11. Ångström absorption exponent (AAE) of coated BCFA ($D_f = 1.7$) with changing fraction of organics (f_{organics}) and mobility diameter (D_{mob}).



585
586
587
588

Figure 12. Ångström absorption exponent (AAE) of pure BCFA ($f_{\text{coating}} = 0\%$) with changing fractal dimension (D_f) and mobility diameter (D_{mob}).



589
590
591

Figure 13. Absorption enhancement factor (E_λ) in BCFA with $D_f = 1.7$, changing fraction of organics (f_{organics}) and mobility diameter (D_{mob}). The top row shows the E_λ derived from the MSTM method whereas the ones derived

592 from Mie code are shown in the bottom row. The enhancement factors are shown for wavelengths equal to 660,
 593 530, and 467nm (right to left).

594

595 3.7 Implications of morphology and composition over black carbon radiative forcing

596

597 In this section, the dependence of the black carbon radiative forcing on modifying composition and morphology
 598 of BCFA is discussed. The relative changes in the top of the atmosphere radiative forcing (ΔF_{TOA}) are quantified
 599 as a function of fractal dimension (D_f) and fraction of organics ($f_{organics}$). It is a sensitivity analysis, applicable
 600 mostly to scenarios with urban pollution having a high mass fraction of combustion aerosols. The black carbon
 601 radiative forcing at the top of the atmosphere (ΔF_{TOA}) is estimated using equation (14) with fixed values of $S_o =$
 602 1368 Wm^{-2} , $N_{cloud}=0.6$, $T = 0.79$, $\tau = 0.03$, and $a = 0.1$ (Chylek and Wong, 1995; Lesins et al., 2002). To focus
 603 primarily on radiative effects of BC, the optical depth τ is taken as 0.03 for smoke aerosol (Penner et al., 1992).
 604 The values of β and ω change with fractal dimension (D_f) and fraction of organics ($f_{organics}$), and are obtained from
 605 the MSTM bulk optical properties. The bulk optical properties are calculated at a wavelength of 530 nm, over a
 606 lognormal polydisperse size distribution with the geometric mean radius (r_o) and standard deviation (σ) fixed to
 607 $0.12\mu\text{m}$ and 1.5, respectively. The details about the bulk optical properties can be found in the supplementary
 608 material of this work.

609 Table. 3 shows how the values of black carbon radiative forcing change for various morphologies represented
 610 by fractal dimension (D_f) for pure black carbon. This can be further understood by the relative change C defined
 611 by:

$$612 \quad C = \frac{\Delta F_{TOA} - \Delta F_{TOA}^{Ref}}{\Delta F_{TOA}^{Ref}} \times 100 \quad (16)$$

613

614 where ΔF_{TOA}^{Ref} is the top of the atmosphere radiative forcing for a reference case where the fractal dimension (D_f)
 615 is 1.7 i.e., a freshly emitted black carbon particle.

616

617 **Table 3.** Black carbon radiative forcing ΔF_{TOA} (Wm^{-2}) calculated for various fractal dimension (D_f) and relative
 618 change (C) with respect to a reference case with $D_f=1.7$.

619

D_f	ΔF_{TOA}	C (%)
1.5	0.704	-1.1
1.6	0.721	-2.3
1.8	0.697	-3.4
1.9	0.681	-5.6
2	0.649	-9.9
2.1	0.608	-15.7
2.2	0.581	-19.4
2.3	0.570	-21.0
2.4	0.507	-29.7
2.5	0.446	-38.2
2.6	0.383	-46.9
2.7	0.324	-55.1
2.8	0.279	-61.2

620

621 Similarly, the values of the black carbon radiative forcing for various compositions represented by fraction of
 622 organics ($f_{organics}$) in a case where the fractal dimension (D_f) is fixed to 2.2 is shown in Table. 4. The values of
 623 relative change (C) are calculated using equation (16) with respect to ΔF_{TOA}^{Ref} as a reference case of zero fraction
 624 of organics ($f_{organics}$) i.e., pure black carbon particle.

625 Global models use the simplified core-shell representation for BC (Bond et al., 2013) which is morphologically
 626 close to a coated BCFA of $D_f=2.8$. In the case of coated BCFA, there is a relative change (C) of 20% when D_f
 627 increases from 1.5 to 2.2. Following the results in Table. 4 the relative change (C) in ΔF_{TOA} of coated BCFA is
 628 also expected to increase as the D_f approaches 2.8. Therefore, the influence of morphology over the ΔF_{TOA} is
 629 considered adequately when using the simplified core-shell representation of BC.

630 It can be seen from from Table 4 that the top of the atmosphere forcing ΔF_{TOA} decreases by up to 55% as the
 631 organic content of the particles increases to 90%. This result is in agreement with the findings of Zeng et al., 2019
 632 where the increasing hygroscopicity of the BC particle results in negative top of the atmosphere forcing. However,
 633 it must be noted that in the study of Zeng et al., 2019, the focus was over aged BC particles with 90-99% coating
 634 fraction and the Santa Barbara DISORT Atmospheric Radiative Transfer (SBDART) model was used for
 635 estimating the radiative forcing.

636 Even though the simplified radiative model for absorbing aerosols used, the results of relative change (C) in
 637 Table 3 and Table 4 can provide insights about the implications of BC ageing on their radiative forcing estimates.
 638 It is demonstrated that the radiative forcing results are highly sensitive towards modifications in morphology and
 639 composition when using the aggregate representation. It must be noted that these results are of high relevance in
 640 the BC hotspots regions of Asia, for example, Manilla in Philippines, where the BC emission shared up to 70%
 641 of calculated PM_{10} (particulate matter with diameter $< 1\mu m$) mass emission factors (Madueno et al., 2019).
 642

643 **Table 4.** Black carbon radiative forcing ΔF_{TOA} (Wm^{-2}) calculated for various fractions of organics ($f_{organics}$) and
 644 relative change (C) with respect to a reference case with $f_{organics} = 0\%$.
 645
 646

$f_{organic}$	ΔF_{TOA}	C (%)
1	0.581	-1.6
5	0.572	-1.5
10	0.572	-2.4
15	0.567	-1.6
20	0.572	-2.4
25	0.567	-1.5
30	0.572	-2.3
40	0.568	-5.1
50	0.552	-10.0
60	0.523	-12.8
70	0.507	-19.0
80	0.471	-32.8
90	0.391	-54.6

647

648 3.8 Parametrization scheme for coated BCFAs

649

650 In this section, the optimal fits for the results of the optical properties obtained from the MSTM code are discussed.
 651 For the extinction and absorption cross-sections, a first order polynomial on logarithmic scales was found to be the
 652 best fit.

653

$$654 \ln C_{ext} = c_0 + c_1 \ln D_{mob} \quad (17)$$

655

$$656 \ln C_{abs} = g_0 + g_1 \ln D_{mob} \quad (18)$$

657

658 For the fittings of scattering cross-section (C_{sca}) and SSA, an equation of the following form was found to fit best.
 659 The asymmetry parameter (g) is well captured by a cubic polynomial in a logarithm space of D_{mob} .

660

$$661 \ln C_{sca} = H_0 + H_1 \ln D_{mob} + H_2 \ln (\ln D_{mob}) \quad (19)$$

662

$$663 \ln SSA = k_0 + k_1 \ln D_{mob} + k_2 \ln (\ln D_{mob}) \quad (20)$$

664

$$665 \ln g = \sum_{n=0}^3 s_n \ln D_{mob}^n \quad (21)$$

666

667 Since the nature of the curve for mass absorption cross-section (MAC_{BC}) changes for various D_i , it was not possible
 668 to find an optimal function representative for the entire dataset. For all the fits, a limitation was found that the
 669 smaller particles are not well represented by the above-mentioned functions. Therefore, in order to find an overall

670 good fit, the data is taken for points with D_{mob} larger than 50nm. Previous studies have also attempted to fit the
 671 optical properties of pure BCFAs with respect to the number of primary particles (N_s) (Smith and Grainger, 2014;
 672 Kahnert, 2012b).

673 In this study, the parametrization scheme is developed for five BC optical properties, the extinction cross-
 674 section C_{ext} , absorption cross-section C_{abs} , scattering cross-section C_{sca} , single scattering albedo SSA , and
 675 asymmetry parameter g with respect to BC size. In total, the fit coefficients for the five BC optical properties are
 676 provided for 192 cases comprising of various combinations of wavelengths (λ), fractal dimensions (D_f) and
 677 fraction of organics (f_{organics}) shown in Fig. 1. For each case, linear regression models were applied individually to
 678 the MSTM modelled optical properties for BC sizes ranging from 10 to 1000nm. The fit coefficients for the five
 679 optical properties in each case are provided in a tabular form as a supplement to this work.

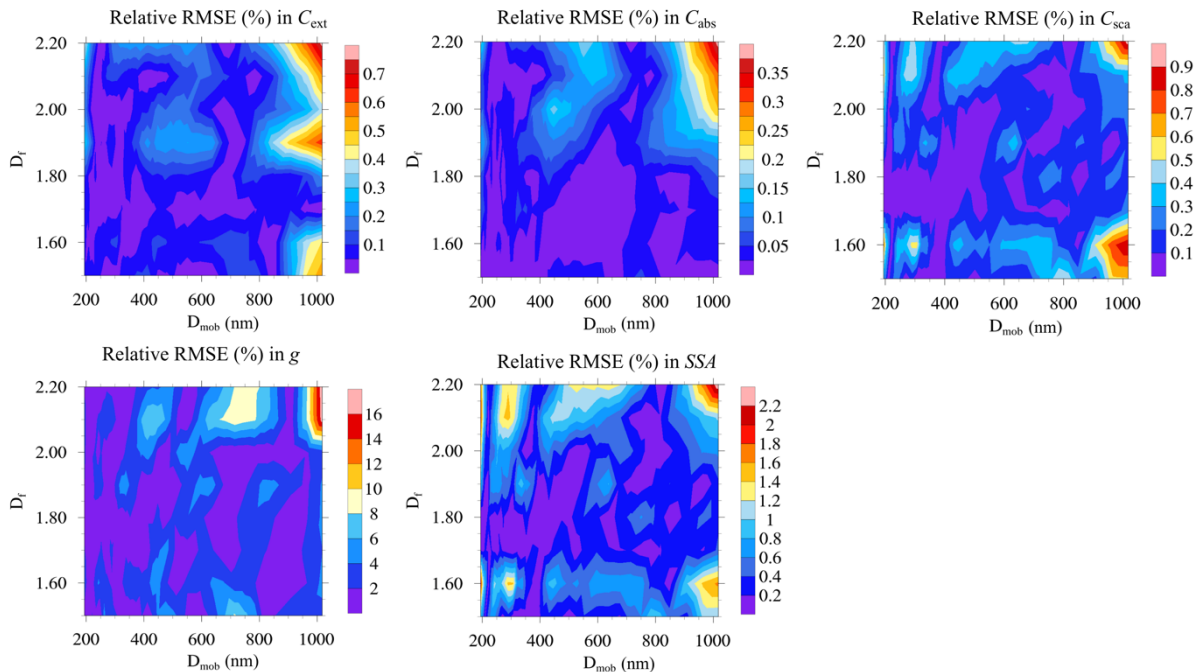
680 The resultant parametrization scheme provides the user an option to estimate the five optical properties at
 681 desired BC size for any of the 192 combinations of λ , D_f , and f_{organics} . It must be noted that the MSTM modelled
 682 optical properties were calculated for fixed values of refractive index because of limited computational resources.
 683 Therefore, the parametrization scheme provided in this study is not able to account for variable refractive indices.
 684

685 3.8.1 Error analysis of the parametrization scheme

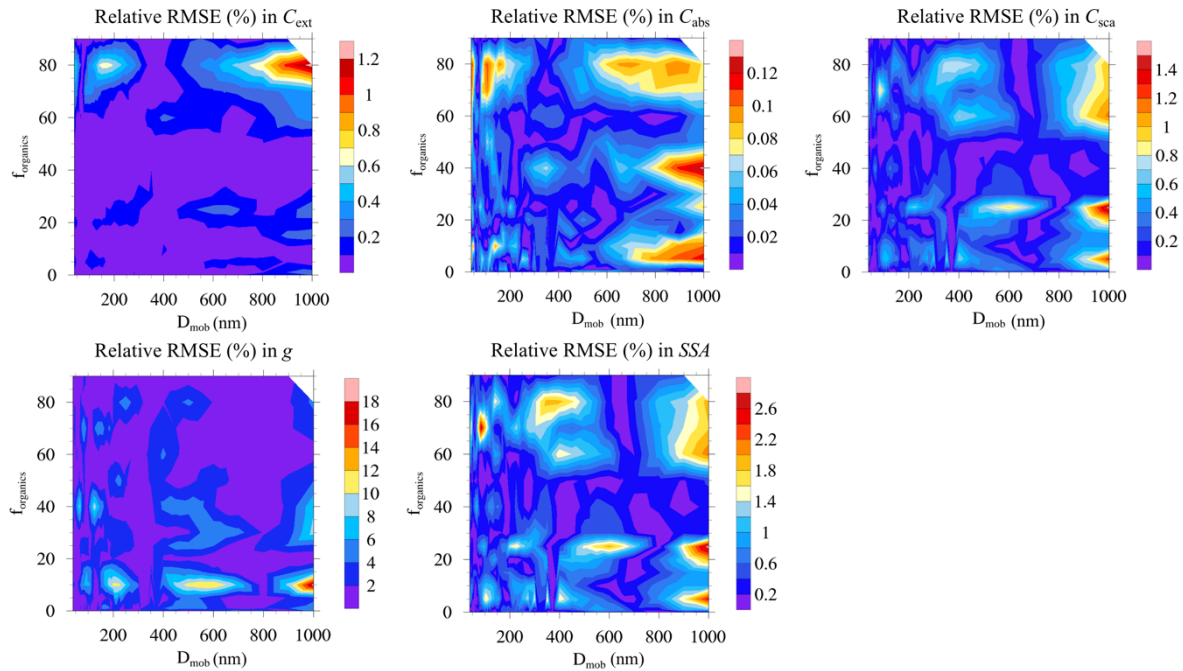
686
 687 In this scheme, the parametrization for optical properties of BCFAs are provided for each point of the classification
 688 given in Fig. 1. In the case of pure BCFAs, the parametrization is provided for all combinations of λ (nm) = {467,
 689 530, 660}, and D_f = {1.5, 1.6, 1.7, 1.8, 1.9, 2.2, 2.1, 2.3, 2.4, 2.5, 2.6, 2.7, 2.8}. Whereas, in the coated BCFAs,
 690 the parametrization scheme is available for combinations of λ (nm) = {467, 530, 660}; D_f = {1.5, 1.6, 1.7, 1.8,
 691 1.9, 2.2} and f_{organics} (%) = {1, 5, 10, 15, 20, 25, 30, 40, 50, 60, 70, 80, 90}. This scheme is named as P_1 and allows
 692 the user an advantage to select among various cases, suitable for their purpose.

693 In order to examine and test the P_1 scheme, the relative root mean square errors (RMSEs) between the MSTM
 694 modelled and fitted values of optical properties were measured. Fig. 14 shows the values of relative RMSEs over
 695 a range of D_{mob} for the cases of λ (nm) = {660}; f_{organics} (%) = {50}; and D_f = {1.5, 1.6, 1.7, 1.8, 1.9, 2.2}. For the
 696 entire range of D_{mob} and D_f , the errors in cross-sections are less than 1%. The relative RMSE is < 2.5% for SSA
 697 and up to 16% for g .

698 Similarly, relative RMSE values for the entire range of f_{organic} can be seen in Fig. 15. For the results shown in
 699 Fig. 15, the case with values of λ (nm) = {660}; D_f = {1.7}; and f_{organics} (%) = {1, 5, 10, 15, 20, 25, 30, 40, 50, 60,
 700 70, 80, 90} were used. The errors in the cross-sections are comparable to Fig. 11, being < 1.5% in all cases.
 701 Similarly, the relative RMSE for SSA is < 3%. The error in g peaks to 18% at f_{organics} < 20% for larger sizes.
 702



703
 704
 705 **Figure 14.** The relative RMSE between MSTM modelled and parametrized values of C_{ext} , C_{abs} , C_{sca} , g , and SSA
 706 for various cases of fractal dimension (D_f) at $\lambda = 660$ nm. In this case, the fraction of organics (f_{organics}) amounts to
 707 50%.



709

710

711

712

713

714

715

716

717

718

719

720

721

722

723

724

725

726

727

Figure 15. The relative RMSE between MSTM modelled and parametrized values of C_{ext} , C_{abs} , C_{sca} , g , and SSA for various cases of fraction of organics ($f_{organics}$) at $\lambda = 660\text{nm}$. The fractal dimension (D_f) is fixed to 1.7.

It is expected, that a dataset of BCFA optical properties with higher resolution for the individual parameters gives better results. To demonstrate this, the P_I scheme is compared to another scheme P_{II} with a reduced dataset. In the P_{II} scheme, the same fits were applied, but optical properties were averaged for D_f in the range from 1.5 to 1.7 and $f_{organics}$ in the range from 60-90% to obtain the “averaged” fit coefficients. The errors from this parametrization scheme P_{II} were compared to the errors from their corresponding cases ($D_f = 1.7$, and $f_{organics} = 60\%$) within the parametrization scheme P_I . The results are summarized in the Table 5. The relative RMSE errors for P_{II} are evidently larger than for P_I , and gives evidence that the dataset with higher resolution minimizes errors when deriving parametrization schemes.

Table 5. Comparison between the Relative RMSE errors of parametrization schemes over a single case of BCFA ($D_f = 1.7$, $f_{organics} = 60\%$, and $\lambda = 660\text{nm}$). The errors on the left (P_I) are for the original scheme developed in this study. Whereas the errors on right show the errors resulting from P_{II} , which is the condensed form of P_I i.e., $D_f = 1.5-1.7$, and $f_{organics} = 60-90\%$.

Optical property	Relative RMSE (%)	
	P_I	P_{II}
C_{ext}	0.09	4.98
C_{abs}	0.02	1.42
C_{sca}	0.30	9.23
g	1.17	8.46
SSA	0.68	7.12

728

729

730

731

732

733

734

735

736

737

4 Conclusions

Optical properties of pure and coated BCFA were systematically investigated as a function of particle size (D_{mob}), primary particle size (a_o), morphology (D_f), composition ($f_{organics}$), and wavelength (λ), developing a parametrization scheme for BCFA optical properties.

Modelled optical properties of BCFA were found to be sensitive to changes in the radius of the primary particle (a_o) at a fixed D_{mob} . The highest sensitivity was seen for cross-sections (C_{ext} , C_{abs} , and C_{sca}), increasing by a factor of almost ten when a_o is changed from 15nm to 30nm, at a fixed D_{mob} . When the volume equivalent radius R_{equ}

738 of a BCFA is fixed, the values of C_{ext} and C_{abs} with changing a_0 were constant, also shown by the study of Kahnert,
739 2016b.

740 In addition to the dependency of BCFA cross-sections over size, a size dependency in optical parameters SSA ,
741 g , and MAC_{BC} was also seen. All the BCFA optical properties showed dependencies over morphology and
742 composition, the nature of this dependencies being specific to each optical property and size dependent. In terms
743 of morphology, the C_{sca} , SSA , and g showed the highest sensitivity towards D_f , pronouncing as the BCFA grows
744 in size. In contrast to the results of C_{sca} , SSA , and asymmetry parameter, the C_{ext} , C_{abs} , and MAC_{BC} were more
745 sensitive with respect to changing composition of BCFA. For e.g., the values of MAC_{BC} increased by a factor of
746 1.5 with increasing amount of f_{organics} up to 90%, at $\lambda = 660\text{nm}$. The optical properties SSA , g , and MAC_{BC} are
747 needed to simulate the BC radiative forcing in global models. Therefore, the simplified core-shell representation
748 of BC in global models does not adequately consider the above discussed impacts of morphology over the BC
749 optical properties.

750 In the visible range, the decrease in the optical properties C_{ext} , C_{abs} , C_{sca} , and MAC_{BC} with λ was large, whereas,
751 a smaller decrease in SSA , and g with λ was shown. The nature of the spectral dependencies with respect to
752 changing morphology and composition varied for various optical properties. While the other optical properties
753 had a less significant spectral dependence on morphology, the asymmetry parameter (g) showed the highest
754 sensitivity, dominant at a higher D_f , i.e., for compact aggregates. For e.g., the ratio of g at $\lambda = 467\text{nm}$ and $\lambda =$
755 660nm changed from 1.1 to 2.6 when going from lower to higher values of D_f . All the cross-sections and black
756 carbon mass absorption cross-section MAC_{BC} showed a significant increase in the spectral dependency with
757 increasing fraction of organics f_{organics} . For e.g., the spectral dependency of MAC_{BC} increased from a factor of 1.97
758 at 1% fraction of organics to a factor of 4 at 90% fraction of organics. It was shown that the MAC_{BC} for a BCFA
759 can be very high for the cases with high organic content, like $20\text{ m}^2/\text{g}$ for 90% fraction of organics at $\lambda = 467\text{nm}$.

760 The dependencies of the Absorption Ångström Exponent (AAE) on morphology and composition were
761 investigated. The values of AAE changed from 1.06 up to 3.6 depending on the fraction of organics (f_{organic}), fractal
762 dimension (D_f), and size (D_{mob}). It is evident from the results, that the AAE of black carbon particle without
763 organic coating can significantly differ to values of about unity, contradicting the interpretation of AAE in some
764 studies. For e.g., the interpretation of the measurement values of $AAE \gg 1$ as biomass burning aerosol might be
765 misleading in the Sandradewi model (Sandradewi et al., 2008). The values of the absorption enhancement factor
766 (E_λ) via coating calculated from the MSTM model varied from 1.0 to 3.0 as a function of wavelength (λ) and size
767 (D_{mob}), whereas, the Mie theory derived E_λ varied from 1.0 to 3.5. The ratio between the MSTM and Mie derived
768 E_λ changed from 1.1 to 1.5 as a function wavelength (λ). The largest discrepancies between the MSTM and Mie
769 derived E_λ was seen at the red wavelength ($\lambda = 660\text{nm}$) due to the presence of Mie resonances in larger particles.

770 The key message of this study is that the sensitivity of various optical properties, especially SSA , g , and MAC_{BC}
771 towards changing morphology and composition can be significant. Further, to understand the atmospheric and
772 climate implications of our findings, a sensitivity study on the black carbon radiative forcing ΔF_{TOA} was
773 conducted. It was shown that the black carbon radiative forcing ΔF_{TOA} (Wm^{-2}) can decrease up to 61% as the
774 BCFA becomes more compact in morphology i.e., a higher fractal dimension (D_f). Therefore, the influence of
775 morphology over the top of the atmosphere radiative forcing is neglected when using the simplified core-shell
776 representation of BC in global model simulations. With respect to changing composition, a decrease of more than
777 50% in ΔF_{TOA} was seen as the organic content of particle increases. These findings are particularly relevant for
778 modelling of polluted urban environments. It is generally assumed that the impact of BC particle becoming more
779 compact, and the increase in organic content are linked. It was shown that the changes in these two ageing factors
780 in tandem result in an overall decrease in the ΔF_{TOA} . Therefore, these factors must be kept under consideration
781 when modelling absorption of BC containing particles and for assessing the radiative impacts using global models.

782 The parametrization scheme provides the user an option to estimate the BC optical properties (extinction cross-
783 section C_{ext} , absorption cross-section C_{abs} , scattering cross-section C_{sca} , single scattering albedo SSA , and
784 asymmetry parameter g) at the desired BC size for various combinations of λ , D_f , and f_{organics} . Even though simple
785 linear regression models were used in this study, the parametrization scheme showed low differences between the
786 parameterized and tabulated MSTM modelled values of optical properties. For the entire parametrization scheme,
787 the relative root mean square errors (RMSEs) in C_{ext} , C_{abs} , and C_{sca} were less than 1%. Similarly, the relative
788 RMSE for SSA was less than 3%. The largest error of about 18% was found in g at f_{organics} less than 20% for larger
789 sizes. It must be noted that the proposed parametrisation scheme is able to accurately predict the BC optical
790 properties above D_{mob} of 50nm under various scenarios not including uncertainties due to a fixed primary particle
791 size and refractive index.

792 It is acknowledged that the results from the parametrization scheme might vary to the results from laboratory
793 and ambient measurements. To understand the nature of discrepancy in modelled optical properties, we encourage

794 users to compare results of this study to results from laboratory or ambient measurements if applicable. It is
795 important to mention that the parametrisation schemes and databases based on realistic representation of BC, like
796 the one developed in this study, is a successful step forward towards a more accurate characterization of BC
797 containing particles and radiative forcing in climate models. Therefore, further studies should be conducted
798 developing more comprehensive databases that include more information on primary particle size, composition,
799 physical variables like hygroscopicity, and optical parameters like refractive indices.

800

801 **Acknowledgement**

802

803 This work is supported by the 16ENV02 Black Carbon project of the European Union through the European
804 Metrology Programme for Innovation and Research (EMPIR).

805

806 **References**

807 Abel, S. J., Haywood, J. M., Highwood, E. J., Li, J. and Buseck, P. R.: Evolution of biomass burning aerosol
808 properties from an agricultural fire in southern Africa, *Geophys. Res. Lett.*, doi:10.1029/2003GL017342,
809 2003.

810 Adachi, K., Chung, S. H. and Buseck, P. R.: Shapes of soot aerosol particles and implications for their effects on
811 climate, *J. Geophys. Res. Atmos.*, doi:10.1029/2009JD012868, 2010.

812 Alexander, D. T. L., Crozier, P. A. and Anderson, J. R.: Brown carbon spheres in East Asian outflow and their
813 radiative propertiesoptical properties, *Science (80-.)*, doi:10.1126/science.1155296, 2008.

814 Appel, B. R., Tokiwa, Y., Hsu, J., Kothny, E. L. and Hahn, E.: Visibility as related to atmospheric aerosol
815 constituents, *Atmos. Environ.*, doi:10.1016/0004-6981(85)90290-2, 1985.

816 Bambha, R. P., Dansson, M. A., Schrader, P. E. and Michelsen, H. A.: Effects of volatile coatings on the laser-
817 induced incandescence of soot, *Appl. Phys. B Lasers Opt.*, doi:10.1007/s00340-013-5463-9, 2013.

818 Berry, M. V., and Percival, I. C.: Optics of fractal clusters such as smoke, *Opt. Act.*, 33, 577-591, doi:
819 10.1080/713821987, 1986.

820 Bescond, A., Yon, J., Ouf, F. X., Ferry, D., Delhaye, D., Gaffié, D., Coppalle, A. and Rozé, C.: Automated
821 determination of aggregate primary particle size distribution by tem image analysis: Application to soot,
822 *Aerosol Sci. Technol.*, doi:10.1080/02786826.2014.932896, 2014.

823 Bockhorn, H.: *Combustion generated fine carbonaceous particles*, KIT Scientific Publishing, Karlsruhe., 2009.

824 Bond, T. C. and Bergstrom, R. W.: Light absorption by carbonaceous particles: An investigative review, *Aerosol*
825 *Sci. Technol.*, doi:10.1080/02786820500421521, 2006.

826 Bond, T. C., Bhardwaj, E., Dong, R., Jogani, R., Jung, S., Roden, C., Streets, D. G. and Trautmann, N. M.:
827 Historical emissions of black and organic carbon aerosol from energy-related combustion, 1850-2000,
828 *Global Biogeochem. Cycles*, doi:10.1029/2006GB002840, 2007.

829 Bond, T. C., Doherty, S. J., Fahey, D. W., Forster, P. M., Berntsen, T., Deangelo, B. J., Flanner, M. G., Ghan, S.,
830 Kärcher, B., Koch, D., Kinne, S., Kondo, Y., Quinn, P. K., Sarofim, M. C., Schultz, M. G., Schulz, M.,
831 Venkataraman, C., Zhang, H., Zhang, S., Bellouin, N., Guttikunda, S. K., Hopke, P. K., Jacobson, M. Z.,
832 Kaiser, J. W., Klimont, Z., Lohmann, U., Schwarz, J. P., Shindell, D., Storelvmo, T., Warren, S. G. and
833 Zender, C. S.: Bounding the role of black carbon in the climate system: A scientific assessment, *J. Geophys.*
834 *Res. Atmos.*, doi:10.1002/jgrd.50171, 2013.

835 Calcote, H. F.: Mechanisms of soot nucleation in flames-A critical review, *Combust. Flame*, doi:10.1016/0010-
836 2180(81)90159-0, 1981.

- 837 Cappa, C. D., Onasch, T. B., Massoli, P., Worsnop, D. R., Bates, T. S., Cross, E. S., Davidovits, P., Hakala, J.,
838 Hayden, K. L., Jobson, B. T., Kolesar, K. R., Lack, D. A., Lerner, B. M., Li, S. M., Mellon, D., Nuaaman,
839 I., Olfert, J. S., Petäjä, T., Quinn, P. K., Song, C., Subramanian, R., Williams, E. J. and Zaveri, R. A.:
840 Radiative absorption enhancements due to the mixing state of atmospheric black carbon, *Science* (80-),
841 doi:10.1126/science.1223447, 2012.
- 842 Chakrabarty, R. K., Moosmueller, H., Chen, L. W. A., Lewis, K., Arnott, W. P., Mazzoleni, C., Dubey, M. K.,
843 Wold, C. E., Hao, W. M., and Kreidenweis, S. M.: Brown carbon in tar balls from smoldering biomass
844 combustion, *Atmos. Chem. Phys.*, 10, 6363-6370, doi: 10.5194/acp-10-6363-2010
- 845 Chakrabarty, R. K., Moosmüller, H., Garro, M. A., Arnott, W. P., Walker, J., Susott, R. A., Babbitt, R. E., Wold,
846 C. E., Lincoln, E. N. and Hao, W. M.: Emissions from the laboratory combustion of wildland fuels: Particle
847 morphology and size, *J. Geophys. Res. Atmos.*, doi:10.1029/2005JD006659, 2006.
- 848 Chen, Y., and Bond, T. C.: Light absorption by organic carbon from wood combustion, *Atmos. Chem. Phys.*, 10,
849 1773-1787, doi: 10.5194/acp-10-1773-2010, 2010.
- 850 China, S., Mazzoleni, C., Gorkowski, K., Aiken, A. C. and Dubey, M. K.: Morphology and mixing state of
851 individual freshly emitted wildfire carbonaceous particles, *Nat. Commun.*, doi:10.1038/ncomms3122, 2013.
- 852 Chylek, P. and Wong, J.: Effect of absorbing aerosols on global radiation budget, *Geophys. Res. Lett.*,
853 doi:10.1029/95GL00800, 1995.
- 854 Cui, X., Wang, X., Yang, L., Chen, B., Chen, J., Andersson, A. and Gustafsson, Ö.: Radiative absorption
855 enhancement from coatings on black carbon aerosols, *Sci. Total Environ.*,
856 doi:10.1016/j.scitotenv.2016.02.026, 2016.
- 857 Doherty, S. J., Warren, S. G., Grenfell, T. C., Clarke, A. D. and Brandt, R. E.: Light-absorbing impurities in Arctic
858 snow, *Atmos. Chem. Phys.*, doi:10.5194/acp-10-11647-2010, 2010.
- 859 Dong, Z., Kang, S., Qin, D., Shao, Y., Ulbrich, S. and Qin, X.: Variability in individual particle structure and
860 mixing states between the glacier-snowpack and atmosphere in the northeastern Tibetan Plateau,
861 *Cryosphere*, doi:10.5194/tc-12-3877-2018, 2018.
- 862 Düsing, S., Wehner, B., Seifert, P., Ansmann, A., Baars, H., Ditas, F., Henning, S., Ma, N., Poulain, L., Siebert,
863 H., Wiedensohler, A. and MacKee, A.: Helicopter-borne observations of the continental background aerosol
864 in combination with remote sensing and ground-based measurements, *Atmos. Chem. Phys.*,
865 doi:10.5194/acp-18-1263-2018, 2018.
- 866 Feng, Y., Ramanathan, V., and Kotamarthi, V. R.: Brown carbon: a significant atmospheric absorber of solar
867 radiation?, *Atmos. Chem. Phys.*, 13, 8607-8621, doi: 10.5194/acp-13-8607-2013, 2013.
- 868 Fierce, L., Riemer, N. and Bond, T. C.: Explaining variance in black carbon's aging timescale, *Atmos. Chem.*
869 *Phys.*, doi:10.5194/acp-15-3173-2015, 2015.
- 870 Fleming, L. T., Lin, P., Roberts, J. M., Selimovic, V., Yokelson, R., Laskin, J., Laskin, A., and Nizkorodov, S.
871 A.: Molecular composition and photochemical lifetimes of brown carbon chromophores in biomass
872 burning organic aerosol, *Atmos. Chem. Phys.*, 20, 1105-1129, doi: 10.5194/acp-20-1105-2020, 2020.
- 873 Forrest, S. R. and Witten, T. A.: Long-range correlations in smoke-particle aggregates, *J. Phys. A Gen. Phys.*,
874 doi:10.1088/0305-4470/12/5/008, 1979.
- 875 Gentner, D. R., Jathar, S. H., Gordon, T. D., Bahreini, R., Day, D. A., El Haddad, I., Hayes, P. L., Pieber, S. M.,
876 Platt, S. M., de Gouw, J., Goldstein, A. H., Harley, R. A., Jimenez, J. L., Prévôt, A. S. H. and Robinson, A.
877 L.: Review of Urban Secondary Organic Aerosol Formation from Gasoline and Diesel Motor Vehicle
878 Emissions, *Environ. Sci. Technol.*, 51(3), 1074–1093, doi:10.1021/acs.est.6b04509, 2017.

- 879 Guarieiro, A. L. N., Eiguren-Fernandez, A., Da Rocha, G. O. and De Andrade, J. B.: An investigation on
880 morphology and fractal dimension of diesel and diesel-biodiesel soot agglomerates, *J. Braz. Chem. Soc.*,
881 doi:10.21577/0103-5053.20160306, 2017.
- 882 Gustafson, B. Å. S. and Kolokolova, L.: A systematic study of light scattering by aggregate particles using the
883 microwave analog technique: Angular and wavelength dependence of intensity and polarization, *J.*
884 *Geophys. Res. Atmos.*, doi:10.1029/1999JD900327, 1999.
- 885 He, C., Liou, K. N., Takano, Y., Zhang, R., Levy Zamora, M., Yang, P., Li, Q. and Leung, L. R.: Variation of the
886 radiative properties optical properties during black carbon aging: Theoretical and experimental
887 intercomparison, *Atmos. Chem. Phys.*, doi:10.5194/acp-15-11967-2015, 2015.
- 888 Hentschel, H. G. E.: Fractal dimension of generalized diffusion-limited aggregates, *Phys. Rev. Lett.*,
889 doi:10.1103/PhysRevLett.52.212, 1984.
- 890 Hess, W. M., Ban, L. L. and McDonald, G. C.: Carbon Black Morphology: I. Particle Microstructure. II.
891 Automated EM Analysis of Aggregate Size and Shape, *Rubber Chem. Technol.*, doi:10.5254/1.3539291,
892 1969.
- 893 Homann, K. H.: Carbon formation in premixed flames, *Combust. Flame*, doi:10.1016/0010-2180(67)90017-X,
894 1967.
- 895 Janssen, N. A. H., Hoek, G., Simic-Lawson, M., Fischer, P., van Bree, L., Brink, H. Ten, Keuken, M., Atkinson,
896 R. W., Ross Anderson, H., Brunekreef, B. and Cassee, F. R.: Black carbon as an additional indicator of the
897 adverse health effects of airborne particles compared with pm10 and pm2.5, *Environ. Health Perspect.*,
898 doi:10.1289/ehp.1003369, 2011.
- 899 Kahnert, M.: Numerically exact computation of the radiative properties optical properties of light absorbing carbon
900 aggregates for wavelength of 200 nm-12.2 μ m, *Atmos. Chem. Phys.*, doi:10.5194/acp-10-8319-2010, 2010.
- 901 Kahnert, M.: On the discrepancy between modeled and measured mass absorption cross sections of light absorbing
902 carbon aerosols, *Aerosol Sci. Technol.*, doi:10.1080/02786821003733834, 2010.
- 903 Kahnert, M.: Optical properties of black carbon aerosols encapsulated in a shell of sulfate: comparison of the
904 closed cell model with a coated aggregate model, *Opt. Express*, doi:10.1364/oe.25.024579, 2017.
- 905 Kim, J., Bauer, H., Dobovičnik, T., Hitznerberger, R., Lottin, D., Ferry, D. and Petzold, A.: Assessing radiative
906 properties optical properties and refractive index of combustion aerosol particles through combined
907 experimental and modeling studies, *Aerosol Sci. Technol.*, doi:10.1080/02786826.2015.1020996, 2015.
- 908 Klimont, Z., Kupiainen, K., Heyes, C., Purohit, P., Cofala, J., Rafaj, P., Borken-Kleefeld, J. and Schöpp, W.:
909 Global anthropogenic emissions of particulate matter including black carbon, *Atmos. Chem. Phys.*,
910 doi:10.5194/acp-17-8681-2017, 2017.
- 911 Kumar, M., Parmar, K. S., Kumar, D. B., Mhawish, A., Broday, D. M., Mall, R. K. and Banerjee, T.: Long-term
912 aerosol climatology over Indo-Gangetic Plain: Trend, prediction and potential source fields, *Atmos.*
913 *Environ.*, doi:10.1016/j.atmosenv.2018.02.027, 2018.
- 914 Lesins, G., Chylek, P. and Lohmann, U.: A study of internal and external mixing scenarios and its effect on aerosol
915 optical properties and direct radiative forcing, *J. Geophys. Res. Atmos.*, doi:10.1029/2001jd000973, 2002.
- 916 Li, J., Liu, C., Yin, Y. and Kumar, K. R.: Numerical investigation on the Ångström exponent of black carbon
917 aerosol, *J. Geophys. Res.*, doi:10.1002/2015JD024718, 2016.
- 918 Liati, A., Brem, B. T., Durdina, L., Vöggtli, M., Dasilva, Y. A. R., Eggenschwiler, P. D. and Wang, J.: Electron
919 microscopic study of soot particulate matter emissions from aircraft turbine engines, *Environ. Sci. Technol.*,
920 doi:10.1021/es501809b, 2014.

- 921 Liu, C., Chung, C. E., Yin, Y. and Schnaiter, M.: The absorption Ångström exponent of black carbon: From
922 numerical aspects, *Atmos. Chem. Phys.*, doi:10.5194/acp-18-6259-2018, 2018.
- 923 Liu, C., Panetta, R. L. and Yang, P.: The influence of water coating on the radiative scattering properties of fractal
924 soot aggregates, *Aerosol Sci. Technol.*, doi:10.1080/02786826.2011.605401, 2012.
- 925 Liu, C., Xu, X., Yin, Y., Schnaiter, M. and Yung, Y. L.: Black carbon aggregates: A database for optical
- 926 Liu, C., Yin, Y., Hu, F., Jin, H. and Sorensen, C. M.: The Effects of Monomer Size Distribution on the Radiative
927 Properties Optical properties of Black Carbon Aggregates, *Aerosol Sci. Technol.*,
928 doi:10.1080/02786826.2015.1085953, 2015.
- 929 Liu, D. T., Whitehead, J., Alfarra, M. R., Reyes-Villegas, E., Spracklen, D. V., Reddington, C. L., Kong, S. F.,
930 Williams, P. I., Ting, Y. C., Haslett, S., Taylor, J. W., Flynn, M. J., Morgan, W. T., McFiggans, G.,
931 Coe, H., and Allan, J. D.: Black-carbon absorption enhancement in the atmosphere determined by
932 particle mixing state, *Nat. Geosci.*, 10, 184-U132, doi: 10.1038/ngeo2901, 2017.
- 933 Liu, D., He, C., Schwarz, J. P., and Wang, X.: Lifecycle of light-absorbing carbonaceous aerosols in the
934 atmosphere, *npj Clim Atmos Sci*, 3, 40, doi: 10.1038/s41612-020-00145-8, 2020.
- 935 Liu, D., He, C., Schwarz, J. P., and Wang, X.: Lifecycle of light-absorbing carbonaceous aerosols in the
936 atmosphere, *npj Clim Atmos Sci*, 3, 40, doi: 10.1038/s41612-020-00145-8, 2020.
- 937 Liu, L. and Mishchenko, M. I.: Scattering and radiative properties optical properties of morphologically complex
938 carbonaceous aerosols: A systematic modeling study, *Remote Sens.*, doi:10.3390/rs10101634, 2018.
- 939 Luo, J., Zhang, Y., Wang, F., Wang, J. and Zhang, Q.: Applying machine learning to estimate the radiative
940 properties optical properties of black carbon fractal aggregates, *J. Quant. Spectrosc. Radiat. Transf.*,
941 doi:10.1016/j.jqsrt.2018.05.002, 2018.
- 942 Luo, J., Zhang, Y., Zhang, Q., Wang, F., Liu, J. and Wang, J.: Sensitivity analysis of morphology on optical
943 properties of soot aerosols, *Opt. Express*, doi:10.1364/oe.26.00a420, 2018.
- 944 Luo, J., Zhang, Y., Zhang, Q., Wang, F., Liu, J. and Wang, J.: Sensitivity analysis of morphology on radiative
945 properties optical properties of soot aerosols, *Opt. Express*, doi:10.1364/oe.26.00a420, 2018.
- 946 Ma, N., Zhao, C. S., Nowak, A., Müller, T., Pfeifer, S., Cheng, Y. F., Deng, Z. Z., Liu, P. F., Xu, W. Y., Ran, L.,
947 Yan, P., Göbel, T., Hallbauer, E., Mildner, K., Henning, S., Yu, J., Chen, L. L., Zhou, X. J., Stratmann,
948 F. and Wiedensohler, A.: Aerosol radiative properties optical properties in the North China Plain during
949 HaChi campaign: An in-situ radiative closure study, *Atmos. Chem. Phys.*, doi:10.5194/acp-11-5959-2011,
950 2011.
- 951 Mackowski, D. W. and Mishchenko, M. I.: A multiple sphere T-matrix Fortran code for use on parallel computer
952 clusters, *J. Quant. Spectrosc. Radiat. Transf.*, doi:10.1016/j.jqsrt.2011.02.019, 2011.
- 953 Mackowski, D. W.: MSTM Version 3.0: April 2013, available at:
954 <http://www.eng.auburn.edu/~dmckwski/scatcodes/> (last access: 10 October 2017), 2013.
- 955 Madueño, L., Kecorius, S., Birmili, W., Müller, T., Simpas, J., Vallar, E., Galvez, M. C., Cayetano, M. and
956 Wiedensohler, A.: Aerosol particle and black carbon emission factors of vehicular fleet in Manila,
957 Philippines, *Atmosphere (Basel)*, doi:10.3390/atmos10100603, 2019.
- 958 Madueño, L., Kecorius, S., Birmili, W., Müller, T., Simpas, J., Vallar, E., Galvez, M. C., Cayetano, M. and
959 Wiedensohler, A.: Aerosol particle and black carbon emission factors of vehicular fleet in Manila,
960 Philippines, *Atmosphere (Basel)*, doi:10.3390/atmos10100603, 2019.
- 961 Mariusz Woźniak. Characterization of nanoparticle aggregates with light scattering techniques. *Optics*
962 [physics.optics]. Aix-Marseille Université, 2012. English. fftel00747711f.

- 963 Michelsen, H. A. Probing Soot Formation, Chemical and Physical Evolution, and Oxidation: A Review of In Situ
964 Diagnostic Techniques and Needs. *Proc. Combust. Inst.* 2017, 36, 717–735.
- 965 Mie, G.: On the optics of turbid media, especially colloidal metal solutions, *Ann. Phys. Berlin*, 1908.
- 966 Mishchenko, M. I., Liu, L., Travis, L. D. and Lacis, A. A.: Scattering and radiative properties optical properties of
967 semi-external versus external mixtures of different aerosol types, *J. Quant. Spectrosc. Radiat. Transf.*,
968 doi:10.1016/j.jqsrt.2003.12.032, 2004.
- 969 Mishchenko, M. I., Travis, L. D. and Lacis, A. a: Scattering, Absorption, and Emission of Light by Small Particles,
970 Vasa, 2002.
- 971 Moosmüller, H., Chakrabarty, R. K. and Arnott, W. P.: Aerosol light absorption and its measurement: A review,
972 *J. Quant. Spectrosc. Radiat. Transf.*, doi:10.1016/j.jqsrt.2009.02.035, 2009.
- 973 Ouf, F. X., Parent, P., Laffon, C., Marhaba, I., Ferry, D., Marcillaud, B., Antonsson, E., Benkoula, S., Liu, X. J.,
974 Nicolas, C., Robert, E., Patanen, M., Barreda, F. A., Sublemontier, O., Coppalle, A., Yon, J., Miserque, F.,
975 Mostefaoui, T., Regier, T. Z., Mitchell, J. B. A. and Miron, C.: First in-flight synchrotron X-ray absorption
976 and photoemission study of carbon soot nanoparticles, *Sci. Rep.*, doi:10.1038/srep36495, 2016.
- 977 Peng, J., Hu, M., Guo, S., Du, Z., Shang, D., Zheng, J., Zheng, J., Zeng, L., Shao, M., Wu, Y., Collins, D. and
978 Zhang, R.: Ageing and hygroscopicity variation of black carbon particles in Beijing measured by a quasi-
979 atmospheric aerosol evolution study (QUALITY) chamber, *Atmos. Chem. Phys.*, doi:10.5194/acp-17-
980 10333-2017, 2017.
- 981 Penner, J. E., Dickinson, R. E. and O'Neill, C. A.: Effects of aerosol from biomass burning on the global radiation
982 budget, *Science* (80-.), doi:10.1126/science.256.5062.1432, 1992.
- 983 Petzold, A., Gysel, M., Vancassel, X., Hitzenberger, R., Puxbaum, H., Vrochticky, S., Weingartner, E.,
984 Baltensperger, U. and Mirabel, P.: On the effects of organic matter and sulphur-containing compounds on
985 the CCN activation of combustion particles, *Atmos. Chem. Phys.*, doi:10.5194/acp-5-3187-2005, 2005.
- 986 properties, *J. Quant. Spectrosc. Radiat. Transf.*, doi: 10.1016/j.jqsrt.2018.10.021, 2019.
- 987 Ramanathan, V. and Carmichael, G.: Global and regional climate changes due to black carbon, *Nat. Geosci.*,
988 doi:10.1038/ngeo156, 2008.
- 989 Rudich, Y., Donahue, N. M. and Mentel, T. F.: Aging of organic aerosol: Bridging the gap between laboratory
990 and field studies, *Annu. Rev. Phys. Chem.*, doi:10.1146/annurev.physchem.58.032806.104432, 2007.
- 991 Safai, P. D., Devara, P. C. S., Raju, M. P., Vijayakumar, K. and Rao, P. S. P.: Relationship between black carbon
992 and associated radiative, physical and radiative properties optical properties of aerosols over two contrasting
993 environments, *Atmos. Res.*, doi:10.1016/j.atmosres.2014.07.006, 2014.
- 994 Sagan, C. and Pollack, J. B.: Anisotropic nonconservative scattering and the clouds of Venus, *J. Geophys. Res.*,
995 doi:10.1029/jz072i002p00469, 1967.
- 996 Saleh, R., Marks, M., Heo, J., Adams, P. J., Donahue, N. M. and Robinson, A. L.: Contribution of brown carbon
997 and lensing to the direct radiative effect of carbonaceous aerosols from biomass and biofuel burning
998 emissions, *J. Geophys. Res.*, doi:10.1002/2015JD023697, 2015. Scarnato, B. V., Vahidinia, S., Richard, D.
999 T. and Kirchstetter, T. W.: Effects of internal mixing and aggregate morphology on radiative
1000 properties optical properties of black carbon using a discrete dipole approximation model, *Atmos. Chem.*
1001 *Phys.*, doi:10.5194/acp-13-5089-2013, 2013.
- 1002 Sandradewi, J., Prévôt, A. S. H., Szidat, S., Perron, N., Alfarra, M. R., Lanz, V. A., Weingartner, E. and
1003 Baltensperger, U. R. S.: Using aerosol light absorption measurements for the quantitative determination

- 1004 of wood burning and traffic emission contribution to particulate matter, *Environ. Sci. Technol.*,
1005 doi:10.1021/es702253m, 2008.
- 1006 Shiraiwa, M., Kondo, Y., Iwamoto, T. and Kita, K.: Amplification of light absorption of black carbon by organic
1007 coating, *Aerosol Sci. Technol.*, doi:10.1080/02786820903357686, 2010.
- 1008 Siegmann, K., Sattler, K. and Siegmann, H. C.: Clustering at high temperatures: Carbon formation in combustion,
1009 *J. Electron Spectros. Relat. Phenomena*, doi:10.1016/S0368-2048(02)00152-4, 2002.
- 1010 Smith, A. J. A. and Grainger, R. G.: Simplifying the calculation of light scattering properties for black carbon
1011 fractal aggregates, *Atmos. Chem. Phys.*, doi:10.5194/acp-14-7825-2014, 2014.
- 1012 Sorensen, C. M.: Light scattering by fractal aggregates: A review, *Aerosol Sci. Technol.*,
1013 doi:10.1080/02786820117868, 2001.
- 1014 Stier, P., Feichter, J., Kinne, S., Kloster, S., Vignati, E., Wilson, J., Ganzeveld, L., Tegen, I., Werner, M.,
1015 Balkanski, Y., Schulz, M. and Boucher, O.: The aerosol-climate model ECHAM5-HAM, *Atmos. Chem.*
1016 *Phys. Discuss.*, doi:10.5194/acpd-4-5551-2004, 2004.
- 1017 Thouy, R. and Jullien, R.: A cluster-cluster aggregation model with tunable fractal dimension, *J. Phys. A. Math.*
1018 *Gen.*, doi:10.1088/0305-4470/27/9/012, 1994.
- 1019 Wang, Y., Chen, Y., Wu, Z., Shang, D., Bian, Y., Du, Z., H. Schmitt, S., Su, R., I. Gkatzelis, G., Schlag, P.,
1020 Hohaus, T., Voliotis, A., Lu, K., Zeng, L., Zhao, C., Rami Alfarra, M., McFiggans, G., Wiedensohler, A.,
1021 Kiendler-Scharr, A., Zhang, Y. and Hu, M.: Mutual promotion between aerosol particle liquid water and
1022 particulate nitrate enhancement leads to severe nitrate-dominated particulate matter pollution and low
1023 visibility, *Atmos. Chem. Phys.*, doi:10.5194/acp-20-2161-2020, 2020.
- 1024 Wang, Y., Liu, F., He, C., Bi, L., Cheng, T., Wang, Z., Zhang, H., Zhang, X., Shi, Z. and Li, W.: Fractal
1025 Dimensions and Mixing Structures of Soot Particles during Atmospheric Processing, *Environ. Sci. Technol.*
1026 *Let.*, doi:10.1021/acs.estlett.7b00418, 2017.
- 1027 Wentzel, M., Gorzawski, H., Naumann, K. H., Saathoff, H. and Weinbruch, S.: Transmission electron
1028 microscopical and aerosol dynamical characterization of soot aerosols, *J. Aerosol Sci.*, doi:10.1016/S0021-
1029 8502(03)00360-4, 2003.
- 1030 Wiedensohler, A., Andrade, M., Weinhold, K., Müller, T., Birmili, W., Velarde, F., Moreno, I., Forno, R.,
1031 Sanchez, M. F., Laj, P., Ginot, P., Whiteman, D. N., Krejci, R., Sellegri, K. and Reichler, T.: Black carbon
1032 emission and transport mechanisms to the free troposphere at the La Paz/El Alto (Bolivia) metropolitan area
1033 based on the Day of Census (2012), *Atmos. Environ.*, 194, 158–169,
1034 doi:https://doi.org/10.1016/j.atmosenv.2018.09.032, 2018.
- 1035 Witten, T. A. and Sander, L. M.: Diffusion-limited aggregation, *Phys. Rev. B*, doi:10.1103/PhysRevB.27.5686,
1036 1983.
- 1037 Wozniak, M., Onofri, F. R. A., Barbosa, S., Yon, J. and Mroczka, J.: Comparison of methods to derive
1038 morphological parameters of multi-fractal samples of particle aggregates from TEM images, *J. Aerosol Sci.*,
1039 doi:10.1016/j.jaerosci.2011.12.008, 2012.
- 1040 Wu, Y., Cheng, T., Liu, D., Allan, J. D., Zheng, L. and Chen, H.: Light Absorption Enhancement of Black Carbon
1041 Aerosol Constrained by Particle Morphology, *Environ. Sci. Technol.*, doi:10.1021/acs.est.8b00636, 2018.
- 1042 Wu, Y., Cheng, T., Zheng, L. and Chen, H.: Models for the radiative simulations of fractal aggregated soot
1043 particles thinly coated with non-absorbing aerosols, *J. Quant. Spectrosc. Radiat. Transf.*,
1044 doi:10.1016/j.jqsrt.2016.05.011, 2016.

- 1045 Zanatta, M., Gysel, M., Bukowiecki, N., Müller, T., Weingartner, E., Areskou, H., Fiebig, M., Yttri, K. E.,
1046 Mihalopoulos, N., Kouvarakis, G., Beddows, D., Harrison, R. M., Cavalli, F., Putaud, J. P., Spindler, G.,
1047 Wiedensohler, A., Alastuey, A., Pandolfi, M., Sellegri, K., Swietlicki, E., Jaffrezo, J. L., Baltensperger, U.
1048 and Laj, P.: A European aerosol phenomenology-5: Climatology of black carbon radiative propertiesoptical
1049 properties at 9 regional background sites across Europe, *Atmos. Environ.*,
1050 doi:10.1016/j.atmosenv.2016.09.035, 2016.
- 1051 Zeng, C., Liu, C., Li, J., Zhu, B., Yin, Y. and Wang, Y.: Optical Properties and Radiative Forcing of Aged BC
1052 due to Hygroscopic Growth: Effects of the Aggregate Structure, *J. Geophys. Res. Atmos.*,
1053 doi:10.1029/2018JD029809, 2019.
- 1054 Zhang, Y., Zhang, Q., Cheng, Y., Su, H., Li, H., Li, M., Zhang, X., Ding, A. and He, K.: Amplification of light
1055 absorption of black carbon associated with air pollution, *Atmos. Chem. Phys.*, doi:10.5194/acp-18-9879-
1056 2018.